

GOODS-*Herschel*: evidence of a UV extinction bump in galaxies at $z > 1$ *

V. Buat¹, E. Giovannoli¹, S. Heinis¹, V. Charmandaris^{2,3,**}, D. Coia⁴, E. Daddi⁵, M. Dickinson⁶, D. Elbaz⁵,
H. S. Hwang⁵, G. Morrison^{7,8}, K. Dasys^{5,**}, H. Aussel⁵, B. Altieri⁴, H. Dannerbauer⁵, J. Kartaltepe⁶, R. Leiton⁵,
G. Magdis⁵, B. Magnelli⁹, and P. Popesso⁹

¹ Laboratoire d'Astrophysique de Marseille, OAMP, Université Aix-Marseille, CNRS, 38 rue Frédéric Joliot-Curie,
13388 Marseille Cedex 13, France
e-mail: veronique.buat@oamp.fr

² University of Crete, Department of Physics and Institute of Theoretical & Computational Physics, 71003 Heraklion, Greece

³ IESL/Foundation for Research & Technology-Hellas, 71110 Heraklion, Greece

⁴ Herschel Science Operation Centre, ESAC, ESA, PO Box 78, 28691 Villanueva de la Cañada, Madrid, Spain

⁵ Laboratoire AIM-Paris-Saclay, CEA/DSM/Irfu – CNRS – Université Paris Diderot, CE-Saclay, 91191 Gif-sur-Yvette, France

⁶ National Optical Astronomy Observatory, 950 North Cherry Avenue, Tucson, AZ 85719, USA

⁷ Institute for Astronomy, University of Hawaii, Honolulu, HI, 96822, USA

⁸ Canada-France-Hawaii telescope, Kamuela, HI, 96743, USA

⁹ Max-Planck-Institut für Extraterrestrische Physik (MPE), Postfach 1312, 85741 Garching, Germany

Received 16 May 2011 / Accepted 5 July 2011

ABSTRACT

Context. Dust attenuation curves in external galaxies are useful for studying their dust properties as well as interpreting their intrinsic spectral energy distributions. These functions are not very well known in the UV range whether at low or high redshift. In particular, the presence or absence of a UV bump at 2175 Å remains an open issue that has consequences on the interpretation of broad band colours of galaxies involving the UV range.

Aims. We want to study the dust attenuation curve in the UV range at $z > 1$ where the UV is redshifted into the visible and with *Herschel* data to constrain dust emission and a global dust attenuation. In particular, we search for a UV bump and related implications for dust attenuation determinations.

Methods. We use deep photometric data of the *Chandra* Deep Field South obtained with intermediate and broad band filters by the MUSYC project to sample the UV rest frame of galaxies with $1 < z < 2$. *Herschel*/PACS and *Spitzer*/MIPS data are used to measure the dust emission. We select 30 galaxies with high S/N in all bands. Their SEDs from the UV to the far-IR are fitted using the CIGALE code and the characteristics of the dust attenuation curves obtained as Bayesian outputs of the SED fitting process.

Results. The mean dust attenuation curve we derive exhibits a significant UV bump at 2175 Å whose amplitude corresponds to 35% (76%) that of the Milky Way (Large Magellanic Cloud: LMC2 supershell) extinction curve. An analytical expression of the average attenuation curve ($A(\lambda)/A_V$) is given and found to be slightly steeper than the Calzetti et al. one, although at a 1σ level. Our galaxy sample is used to study the derivation of the slopes of the UV continuum from broad band colours, including the rest frame GALEX *FUV* – *NUV* colour. Systematic errors induced by the presence of the bump are quantified. We compare dust attenuation factors measured with CIGALE to the slope of the UV continuum and find that there is a large scatter around the relation valid for local starbursts (~ 0.7 mag). The uncertainties on the determination of the UV slope lead to an extra systematic error in a range of 0.3 to 0.7 mag on dust attenuation when a filter overlaps the UV bump.

Key words. galaxies: high-redshift – galaxies: ISM – ultraviolet: galaxies – infrared: galaxies – dust, extinction

1. Introduction

Stellar light in galaxies is absorbed and scattered by the interstellar medium, because of the presence of dust grains. On a galaxy scale, the process is usually quantified by introducing an average attenuation function that reflects the combined effects of absorption and scattering in a complex geometry.

The most important feature in the extinction curves of the Milky Way (MW) and Large Magellanic Cloud (LMC) is the so-called UV bump, a strong absorption feature at 2175 Å that

is not observed in the Small Magellanic Cloud (SMC) bar, although a line of sight through the SMC wing exhibits an extinction curve with a strong UV bump (Li & Draine 2002; Cartledge et al. 2005). The exact origin of this feature is still under discussion (e.g. Draine 1989; Xiang et al. 2011, and references therein). When dealing with average attenuation curves, the search for a bump is complicated by the effects of scattering or geometry (Inoue et al. 2006; Noll et al. 2007; Panuzzo et al. 2007), which may affect the amplitude of the resulting bump on an average attenuation curve, even when assuming a local Milky Way-like extinction curve.

The best way to study UV bumps in external galaxies is to perform UV rest frame spectroscopy. Calzetti et al. (1994) deduced the net attenuation curves of local starburst galaxies by

* Appendix A is available in electronic form at <http://www.aanda.org>

** Chercheur Associé, Observatoire de Paris, LERMA (CNRS: UMR8112), 61 Av. de l'Observatoire, 75014 Paris, France.

comparing the UV spectra of dusty and dust-free spectra of local starbursts and they did not find any bump. Conversely, Noll et al. (2005, 2009a) observed a significant 2175 Å absorption feature in the spectra of star-forming galaxies at $z \sim 2$, consistent with an extinction curve midway between the SMC and LMC ones.

The 2175 Å feature has also been detected in the spectral energy distribution (SED) of some distant galaxies hosting gamma-ray bursts (Liang & Li 2009, 2010) and the extinction curves are found to display a wide diversity of shapes (Liang & Li 2009, 2010; Zafar et al. 2011, and references therein). We also refer to Xiang et al. (2011) for an extensive review of the detections of the UV bump in Galactic and extragalactic interstellar media.

Broad band colours are also used to search for evidence of a UV bump. From an analysis of the observed $B - R$ colours of galaxies at $z \sim 1$ Conroy (2010) speaks against any UV bumps as strong as the one in the Milky Way, whereas Burgarella et al. (2005) analysed the broad bands SEDs of nearby galaxies observed by GALEX and IRAS and conclude to there is a bump in the attenuation curve of these galaxies. In all cases, the use of broad band colours that overlap the bump makes it difficult to disentangle the effects of a dust extinction curve with or without a bump of dust/stars geometry and of various star formation histories (Inoue et al. 2006; Panuzzo et al. 2007; Johnson et al. 2007a,b; Buat et al. 2011), leading to contradicting conclusions on the presence of a UV bump in nearby galaxies observed by GALEX and SDSS (Conroy et al. 2010; Johnson et al. 2007a,b).

The presence and characteristics of both the UV bump and the far UV rise in the extinction and attenuation curves can provide information on the interstellar medium properties (Noll et al. 2009a). Beyond the studies of the interstellar medium, a reliable attenuation curve in the UV range is very useful for deriving star formation rates in galaxies since the UV emission is commonly used as a star formation tracer. For example, Wijesinghe et al. (2010) compared star formation rates deduced from luminosities measured in the GALEX bands and the H α and [OII] emission lines and concluded that they must remove the 2175 Å feature from the attenuation curve to obtain the best agreement between the different star formation rate estimators. The attenuation curve of Calzetti et al. (2000) is commonly used, especially in high- z studies and does not include a bump. If such a bump is present, omitting it leads to incorrect dust attenuation corrections (Ilbert et al. 2009).

The global amount of dust attenuation is robustly estimated by comparing dust and stellar emission, through the $L_{\text{IR}}/L_{\text{UV}}$ ratio. When IR data are not available, the shape of the UV continuum (<3000 Å) has been proposed as a proxy to measure the amount of attenuation. Calzetti et al. (1994) have shown that the UV continuum of local starburst galaxies can be fit by a power law ($f_{\lambda}(\text{erg cm}^{-2} \text{s}^{-1} \text{Å}^{-1}) \propto \lambda^{\beta}$) for $\lambda > 1200$ Å. They calculated β by defining ten windows in the IUE spectra of their galaxies avoiding the 2175 Å feature. Meurer et al. (1999) have found a relation between β and the amount of dust attenuation measured by $L_{\text{IR}}/L_{\text{UV}}$. This local starburst relation is widely used to estimate dust attenuation in high-redshift galaxies using a broad band colour in the UV rest frame of the galaxies as a proxy of β (e.g. Burgarella et al. 2007; Elbaz et al. 2007; Daddi et al. 2007; Reddy et al. 2008). If a bump is present in the dust attenuation curve, one must be cautious by choosing broad band filters that do not overlap the bump in order to estimate reliable slopes outside the wavelength range affected by the bump, as was done to derive the Meurer et al. (1999) relation. This has been illustrated by studies of the local universe based on GALEX FUV and NUV data: the NUV band largely overlaps the UV bump

and the FUV-NUV colour is found to be sensitive to the presence or absence of this feature as well as to the recent star formation history (Panuzzo et al. 2007; Inoue et al. 2006).

In this paper we take advantage of the availability of high quality deep optical data obtained through intermediate-band filters in the *Chandra* Deep Field South (CDFS) to sample the rest frame UV of galaxies at high redshift. These data are combined with the *Herschel* observations of the CDFS field as part of the open-time key programme GOODS-*Herschel* project (P.I. D. Elbaz). The galaxies detected in the far-IR are expected to experience a substantial extinction that helps to detect the imprint of the bump in their SED. The combination of UV and IR data will allow us to compare the properties of the UV continuum to the dust attenuation at work in these objects. In a similar vein, Ilbert et al. (2009) use broad and intermediate band filters to derive photometric redshifts in the COSMOS field and find that a UV bump is necessary to explain the UV rest frame fluxes of some starburst galaxies, but they do not discuss the amplitude of the bump and dust attenuation in these galaxies.

The construction of the sample is explained in Sect. 2. We want to use only sources detected with high signal-to-noise ratio (SNR) in a large number of filters, which sample the rest frame UV wavelength region affected by the bump well. This criterium leads to a redshift selection between 0.95 and 2.2. The dust attenuation curve, as well as the amount of dust obscuration, is constrained by fitting the whole SEDs of the galaxies with the CIGALE code, which is described in Sect. 3. Section 4 is devoted to the results about the presence of the UV bump and Sect. 5 to the consequences on determining the slope of the UV continuum and dust attenuation in galaxies. The conclusions are presented in Sect. 6.

2. Selection of the sample

As part of the GOODS-*Herschel* key programme (Elbaz et al. 2011), the *Herschel* Space Observatory (Pilbratt et al. 2010) surveyed a small area of the Great Observatories Origins Deep Survey Southern field (GOODS-S): $10' \times 10'$ centred on the CDFS were observed at 100 and 160 μm over 264 h by the PACS instrument (Poglitsch et al. 2010). Source extraction on the PACS images was performed at the prior position of *Spitzer* 24 μm sources as described in Elbaz et al. (2011).

Cardamone et al. (2010, the MUSYC project) compiled a uniform catalogue of optical and infrared photometry for sources in GOODS-S, incorporating the GOODS *Spitzer* IRAC and MIPS data (Dickinson et al. 2003). In particular, they used deep intermediate-band imaging from the Subaru telescope to provide photometry with finer wavelength sampling than is possible from standard broad band data. This was done in part to enable more accurate photometric redshifts, but for our purposes here it provides a valuable means of tracing the detailed shape of the UV rest frame spectrum and to look for the presence of a UV absorption bump.

We started with the GOODS-*Herschel* catalogue of 533 sources detected at 100 μm , and identify 325 sources with an SNR (flux over error) at 100 μm greater than 5. We restricted the sample further to the 235 sources also detected at 160 μm with an $SNR > 3$, and we cross-correlated them with the MUSYC catalogue of 84 402 sources with photometric redshifts. The tolerance radius between IRAC and optical coordinates was taken to be 2 arcsec and it results in a sample of 219 cross-matched sources. Total fluxes in optical and *Spitzer* bands were computed from aperture fluxes as described in Cardamone et al. (2010).

Table 1. Galaxy sample.

| N | RA (2000) deg | Dec (2000) deg | z | $\log(L_{\text{IR}})$ L_{\odot} | A_{UV} mag | E_b | err_{E_b} | γ Å | err_{γ} Å | δ | err_{δ} | χ^2_{min} |
|-----------------|------------------|-------------------|-------------------|--------------------------------------|------------------------|-------|-------------|---------------|---------------------|----------|----------------|-----------------------|
| 1 | 03:32:36.19 | -27:42:58.2 | 0.967 | 11.45 | 1.14 | 0.98 | 0.67 | 339.32 | 107.00 | 0.09 | 0.03 | 3.16 |
| 2 | 03:32:20.72 | -27:44:53.7 | 0.969 | 11.50 | 2.80 | 1.74 | 0.31 | 361.66 | 102.58 | -0.30 | 0.00 | 2.69 |
| 3 | 03:32:16.45 | -27:44:48.7 | 0.976 | 11.49 | 2.98 | 1.15 | 0.61 | 348.02 | 107.33 | 0.03 | 0.07 | 2.63 |
| 4 | 03:32:31.80 | -27:49:58.4 | 0.98 ² | 11.49 | 2.89 | 1.18 | 0.54 | 360.33 | 107.93 | -0.16 | 0.09 | 1.43 |
| 5 | 03:32:42.28 | -27:47:46.1 | 0.998 | 11.43 | 1.98 | 1.68 | 0.34 | 376.98 | 101.85 | -0.20 | 0.12 | 2.31 |
| 6 | 03:32:37.39 | -27:44:07.0 | 1.018 | 11.28 | 3.90 | 1.51 | 0.46 | 350.17 | 106.16 | -0.24 | 0.06 | 1.76 |
| 7 | 03:32:06.43 | -27:47:28.7 | 1.021 | 11.69 | 3.75 | 1.25 | 0.54 | 370.61 | 106.19 | -0.29 | 0.03 | 2.30 |
| 8 ¹ | 03:32:15.78 | -27:46:30.2 | 1.023 | 11.35 | 1.68 | 1.05 | 0.65 | 347.67 | 107.83 | -0.21 | 0.05 | 3.72 |
| 9 | 03:32:36.02 | -27:44:23.8 | 1.038 | 11.34 | 1.98 | 1.55 | 0.45 | 351.24 | 106.58 | -0.02 | 0.05 | 1.65 |
| 10 | 03:32:10.58 | -27:47:06.1 | 1.045 | 11.42 | 2.83 | 0.95 | 0.62 | 352.28 | 108.69 | -0.10 | 0.09 | 1.24 |
| 11 | 03:32:28.98 | -27:49:08.2 | 1.094 | 11.59 | 2.01 | 1.63 | 0.43 | 375.24 | 102.58 | -0.29 | 0.02 | 5.58 |
| 12 | 03:32:39.87 | -27:47:15.0 | 1.095 | 11.43 | 1.93 | 1.79 | 0.29 | 400.42 | 92.73 | -0.27 | 0.07 | 2.25 |
| 13 | 03:32:25.86 | -27:50:19.6 | 1.095 | 11.52 | 2.40 | 1.42 | 0.52 | 355.97 | 106.19 | -0.16 | 0.06 | 2.30 |
| 14 ¹ | 03:32:17.18 | -27:52:20.5 | 1.097 | 12.09 | 5.61 | 1.03 | 0.39 | 368.57 | 104.51 | -0.30 | 0.02 | 4.56 |
| 15 | 03:32:34.85 | -27:46:40.5 | 1.099 | 11.46 | 4.19 | 1.61 | 0.43 | 373.69 | 102.00 | -0.18 | 0.08 | 1.08 |
| 16 | 03:32:34.63 | -27:53:24.5 | 1.107 | 11.61 | 2.47 | 1.04 | 0.64 | 344.75 | 107.87 | -0.03 | 0.10 | 1.12 |
| 17 ¹ | 03:32:29.97 | -27:45:29.8 | 1.209 | 12.07 | 1.13 | 0.87 | 0.67 | 328.56 | 106.76 | 0.08 | 0.04 | 15.92 |
| 18 | 03:32:43.48 | -27:45:56.5 | 1.220 | 11.45 | 2.54 | 1.35 | 0.55 | 336.36 | 105.68 | -0.21 | 0.06 | 2.70 |
| 19 | 03:32:47.17 | -27:51:06.1 | 1.224 | 11.82 | 4.66 | 1.10 | 0.50 | 337.70 | 107.00 | -0.29 | 0.03 | 1.22 |
| 20 ¹ | 03:32:35.97 | -27:48:50.4 | 1.309 | 11.54 | 1.24 | 0.87 | 0.67 | 337.88 | 107.68 | 0.02 | 0.07 | 2.70 |
| 21 ¹ | 03:32:29.93 | -27:43:01.0 | 1.37 ² | 12.12 | 4.29 | 1.62 | 0.32 | 408.06 | 89.38 | 0.01 | 0.06 | 1.71 |
| 22 ¹ | 03:32:28.79 | -27:47:55.6 | 1.383 | 11.69 | 4.02 | 0.66 | 0.47 | 331.44 | 107.91 | -0.21 | 0.07 | 3.36 |
| 23 | 03:32:34.03 | -27:50:28.8 | 1.384 | 11.82 | 3.32 | 1.45 | 0.38 | 369.56 | 102.64 | 0.08 | 0.04 | 2.50 |
| 24 | 03:32:41.33 | -27:45:38.2 | 1.52 ² | 11.91 | 3.69 | 1.30 | 0.51 | 332.05 | 107.31 | -0.20 | 0.08 | 1.53 |
| 25 ¹ | 03:32:37.76 | -27:52:12.3 | 1.609 | 12.33 | 4.63 | 1.03 | 0.51 | 333.88 | 111.60 | -0.04 | 0.05 | 6.39 |
| 26 | 03:32:37.71 | -27:50:00.4 | 1.619 | 12.43 | 5.21 | 0.94 | 0.36 | 352.65 | 105.73 | -0.09 | 0.07 | 2.88 |
| 27 | 03:32:17.82 | -27:46:39.7 | 1.956 | 11.93 | 2.85 | 0.83 | 0.60 | 368.08 | 107.77 | 0.01 | 0.08 | 1.69 |
| 28 | 03:32:41.77 | -27:46:56.4 | 1.994 | 12.00 | 3.32 | 1.03 | 0.50 | 351.00 | 107.88 | 0.02 | 0.09 | 2.85 |
| 29 | 03:32:40.05 | -27:47:55.4 | 1.997 | 12.40 | 3.79 | 1.39 | 0.40 | 328.89 | 103.03 | -0.13 | 0.10 | 2.30 |
| 30 | 03:32:40.75 | -27:49:26.1 | 2.130 | 12.12 | 3.02 | 1.33 | 0.53 | 350.01 | 107.06 | -0.08 | 0.11 | 1.41 |

Notes. IR luminosities ($\log(L_{\text{IR}})$), dust attenuation (A_{UV}) and parameters relative to the attenuation curve (the amplitude and width of the UV bump, E_b and γ , and the steepness of the curve, δ) and their corresponding errors are obtained from the Bayesian analysis performed with CIGALE. ⁽¹⁾ X-ray emitter. ⁽²⁾ No spectroscopic redshift, the photometric redshift is used.

Before selecting sources according to their redshift we had to chose the bands to use: the redshift range was selected to ensure a good sampling of the UV range. All the optical broad bands of the MUSYC survey were considered (U , $U38$, B , V , R , I , z) and J , H , K bands were added when available. We also added data from intermediate-band filters whose 5σ depth was fainter than 25 ABmag (Table 2 of Cardamone et al. 2010). In practice we used IA-427, 445, 484, 505, 527, 550, 574, 598, 624, 651, 679 and 738. Figure 1 illustrates the rest frame wavelengths corresponding to these filters as a function of z .

In order to ensure a good photometric sampling around the UV bump (2175 Å) we selected galaxies with redshifts between 0.95 and 2.2. In this redshift range we have more than ten photometric bands available in the UV (1300–3000 Å) and a good sampling around 2175 Å (Fig. 1). Seventy-six galaxies fulfil the redshift condition. To ensure that sources at $z < 1.6$ have data below rest frame 1800 Å, they must have been detected in the U and U38 filters above 5σ (see Table 3 of Cardamone et al. 2010). This leads us to 39 galaxies, all of which are also strongly detected in the other broad bands, as well as above 5σ in the IA-427 filter. When $z > 1.6$, measurements beyond the U filter are sufficient, we selected sources detected with $SNR > 5$ in the B band, adding an additional constraint of a 5σ detection an

intermediate filter (IA-427 for $z < 1.8$ and IA-484 for $z > 1.8$), 13 galaxies are thus added to the selection. At the end we had selected 52 galaxies. As a further check, we retrieved the HST images at the coordinates of these 52 sources using the GOODS cutout service V2.0 provided by the Multimission Archive at STScI (<http://archive.stsci.edu>). We discard 22 sources with bright neighbours closer than 4 arcsec to the *Herschel* detection and with IR measurements that are uncertain (the full width half maximum ($FWHM$) of the point spread function at 100 μm is 6.7 arcsec). Half of the remaining sample of 30 galaxies has a disk-like morphology, the other half is dominated by compact sources with few interacting-peculiar galaxies, while 28 have spectroscopic redshifts. The sample of galaxies is presented in Table 1. The HST images for each target are available as online material. Seven galaxies are identified as X-ray emitters by Cardamone et al. (2008) and are flagged in Table 1.

As described earlier in this section, the present study is based on galaxies that are strongly detected from the UV to the far-IR and whose rest frame UV spectrum is sampled by several intermediate-band filters. These highly selective criteria lead to a rather small sample of objects that we study in detail in this paper in order to derive the parameters of a dust attenuation curve. Our analysis is complementary to other studies at intermediate and

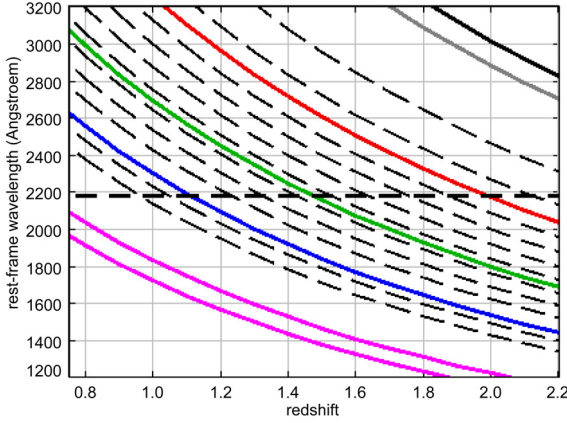


Fig. 1. Rest frame ultraviolet wavelengths sampled with our dataset as a function of redshift. The solid curves correspond to broad band filters (from bottom left corner to top right corner: *U*, *U38*, *B*, *V*, *R*, *I* and *z*) and the dashed curves to intermediate-band filters (from bottom left corner to top right corner: IA-427, 445, 484, 505, 527, 550, 574, 598, 624, 651 (coincident with the red solid curve for the *R*-band), 679 and 738. The *FWHM* of the intermediate filters varies from 20 to 34 nm. The horizontal dotted line corresponds to 2175 Å, the central wavelength of the expected bump.

high redshifts that are based on larger samples, but they lack far-IR data. These studies have concluded that a UV bump must be introduced in the attenuation curve, but they were unable to quantify either the amplitude of the bump or the modification of the attenuation curve (Ilbert et al. 2009; Kriek et al. 2011).

3. SED fitting with CIGALE

SED fitting is performed with the CIGALE code (Code Investigating GALaxy Emission) developed by Noll et al. (2009b). This is a physically-motivated code that derives properties of galaxies by fitting their UV-to-far-IR SEDs. CIGALE combines a UV-optical stellar SED and a dust, IR-emitting component and fully conserves the energetic balance between the dust absorbed stellar emission and its re-emission in IR. We refer to Giovannoli et al. (2011) for details on the use of CIGALE to fit SEDs of actively star-forming galaxies observed both in UV and far-IR (rest frame). In the present work, the sampling of the UV range is very good so we expect to constrain the dust attenuation curve. To model the attenuation by dust, the code uses the attenuation law of Calzetti et al. (2000) as a baseline, and offers the possibility of varying the steepness of this law and adding a bump centred at 2175 Å. We refer to Noll et al. (2009b) for a complete description of the dust attenuation prescription. The dust attenuation is described as

$$A(\lambda) = \frac{A_V}{4.05} (k'(\lambda) + D_{\lambda_0, \gamma, E_b}(\lambda)) \left(\frac{\lambda}{\lambda_V} \right)^\delta, \quad (1)$$

where $\lambda_V = 5500$ Å, $k'(\lambda)$ comes from Calzetti et al. (2000) (Eq. (4)) and $D_{\lambda_0, \gamma, E_b}(\lambda)$, the Lorentzian-like Drude profile commonly used to describe the UV bump (Fitzpatrick & Massa 1990; Noll et al. 2009a) is defined as

$$D_{\lambda_0, \gamma, E_b} = \frac{E_b \lambda^2 \gamma^2}{(\lambda^2 - \lambda_0^2)^2 + \lambda^2 \gamma^2}. \quad (2)$$

The peak amplitude above the continuum, *FWHM* and central wavelength of the bump (E_b , γ and λ_0) are free parameters of the

code¹. There is no indication for variations in the central wavelength of the bump either in the Milky Way or in external galaxies (Noll et al. 2009a, and references therein), therefore we fix the central wavelength of the bump λ_0 to 2175 Å. The parameter γ , indicating the *FWHM*, can vary between 200 and 500 Å in order to cover the range of values found in previous studies. The *FWHM* found in the Milky Way is 437 Å (Fitzpatrick & Massa 2007), while Noll et al. (2009a) found a *FWHM* of 274 Å for their composite spectrum of galaxies with $1.5 < z < 2.5$. After several trade-offs, the amplitude of the bump E_b is chosen between 0 and 2. For comparison, the corresponding value for the extinction curve of the Milky Way is 3.52 (Fitzpatrick & Massa 2007), 1.63 for the LMC2 supershell (Gordon et al. 2003), and between 0.5 and 1 for $z \sim 2$ galaxies (Noll et al. 2009a).

Finally we select δ between -0.3 and 0.1 , and this range of values is also chosen after several trade-offs, excluding values never chosen by the code.

The stellar population created by CIGALE is the combination of an old, exponentially decreasing, component (starting at the age of the universe at the redshift of the galaxy) and a young burst of constant star formation beginning between 0.3×10^8 and 3×10^8 years ago. The e-folding rate of the old stellar population is found to be 2 ± 0.4 Gyr. Since the UV emission reaches a stationary state after $\sim 10^8$ years of constant star formation, the general shape of the UV SEDs analysed in this work is predominantly modified by the effect of dust attenuation (Calzetti et al. 1994).

The attenuation correction is applied to each component. To take the different distributions of stars of different ages into account, we adopt a visual attenuation A_V for the old stellar component equal to half what is used for the young component. The exact value of this reduction factor (called f_{att} in the code) is very difficult to constrain even if a value lower than 1 is always found (Noll et al. 2009b; Buat et al. 2011). In a first step we ran CIGALE with f_{att} as a free parameter with values comprised between 0 and 1, we obtained a mean value of 0.5 for f_{att} . To reduce the computation time we decided to freeze the value of f_{att} , after checking that it did not modify the values obtained for the other output parameters of the code.

Dust luminosities ($\log(L_{\text{IR}})$ between 8 and 1000 μm) are computed by fitting Dale & Helou (2002) templates and are linked to the attenuated stellar population models (the stellar luminosity absorbed by the dust is re-emitted in IR). The validity of Dale & Helou (2002) templates for measuring total IR luminosities of sources detected by *Herschel* is confirmed by the studies of Elbaz et al. (2010, 2011). Non-thermal sources, not linked to the absorbed stellar population, can also contribute to the dust emission. CIGALE includes dust-enshrouded AGNs by adding two PAH-free templates from Siebenmorgen et al. (2004) as described in Buat et al. (2011). These two templates differ by the amount of silicate absorption, and their spectral distribution beyond 20 microns is similar to the mean template constructed by Mullaney et al. (2011). The spectrum below 20 microns is representative of type 2 AGNs.

The AGN contribution to L_{IR} is found to be lower than 10% except for both N-17, the only X-ray source of our sample with broad emission lines, and N-25 that has the highest X-ray luminosity ($\log(L_X/L_\odot) = 44.4$) and exhibits a power law SED. For these two sources the AGN fraction is found to be greater than 50%. The current version of CIGALE is unable to fit these SEDs accurately leading to minimum χ^2 values equal to 16 and

¹ E_b and γ are related to the original parameters c_3 and γ_{FM} introduced by Fitzpatrick & Massa (1990): $E_b = c_3/\gamma_{\text{FM}}^2$ and $\gamma = \gamma_{\text{FM}} \times \lambda_0^2$.

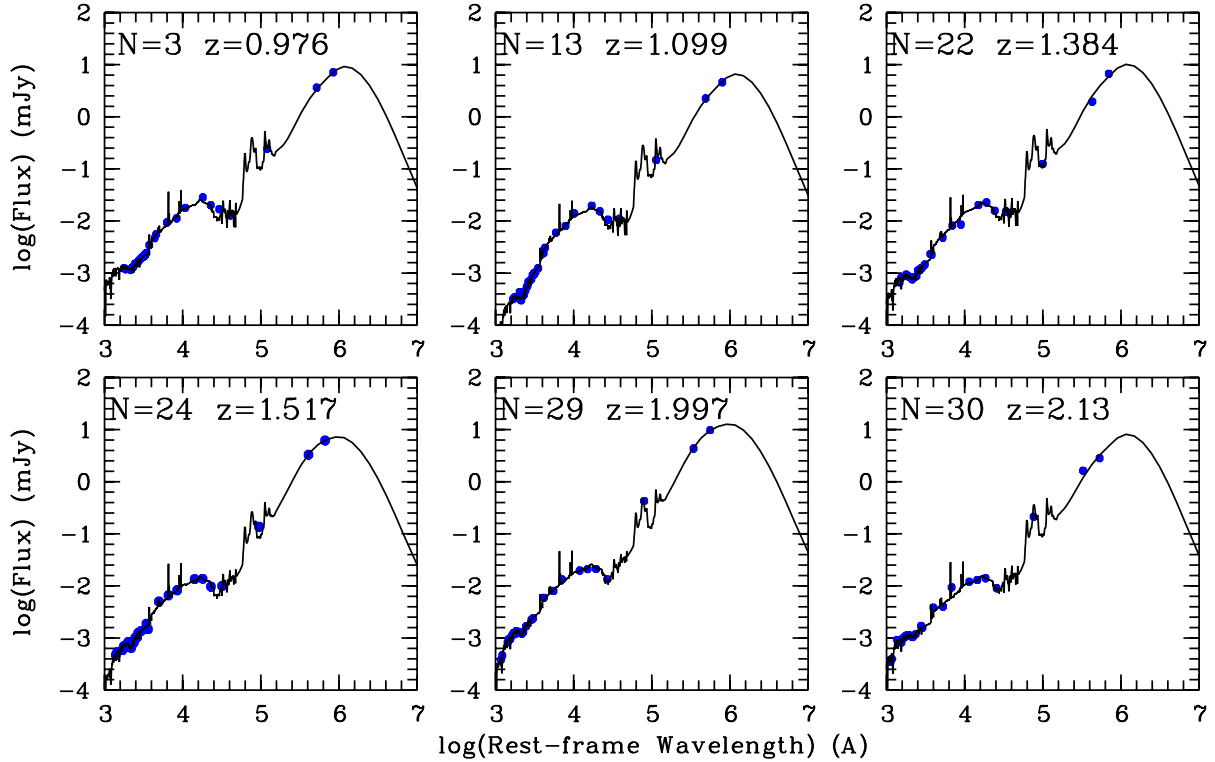


Fig. 2. Examples of SEDs fitted with CIGALE. The best model (χ^2 minimization) is plotted together with the observed fluxes.

6.4 for N-17 and N-25, respectively. These two sources will be discarded when the output parameters of the code are discussed. The case of the other X-ray sources is discussed in Sect. 4.2. Examples of full SED fitting are shown in Fig. 2. The figures for the full sample are available as online material.

All the output parameters are estimated through Bayesian analysis. Results for the total IR luminosity, L_{IR} , the dust attenuation at 1530 \AA , A_{UV} , and the peak amplitude of the bump, E_b , are listed in Table 1 together with their errors, also evaluated by a Bayesian calculation (Giovannoli et al. 2011). The range of $\log(L_{\text{IR}}/L_{\odot})$ is 11.25–12.4: all the sources are luminous infrared galaxies ($\log(L_{\text{IR}}/L_{\odot}) > 11$, LIRG) or ultra-luminous infrared galaxies ($\log(L_{\text{IR}}/L_{\odot}) > 12$, ULIRG). The mean dust attenuation is found to be quite large with $\langle A_V \rangle = 0.92 \pm 0.34$ mag and $\langle A_{\text{UV}} \rangle = 3.09 \pm 1.11$ mag. This large dust attenuation is expected for LIRGs and ULIRGs and is favourable to searching for the imprint of UV bumps in the spectrum of these galaxies.

4. Evidence of a bump at 2175 \AA

4.1. Amplitude of the bump from SED fitting with CIGALE

Some examples of SEDs in the UV range are shown in Fig. 3. The figures for the whole sample are available in Appendix A (online material). These few examples show the excellent sampling of the UV SED achieved thanks to using medium filters. A dip at 2175 \AA is clearly seen in most of the observed SEDs. The best models obtained by the χ^2 minimization are found to reproduce the data very well. They all correspond to a bump amplitude over 0. The median value of E_b for the best models is 1.5. In Fig. 4 the Bayesian estimate of E_b is plotted against the redshift of the sources. All the sources are found to exhibit a bump. The uncertainty given by the Bayesian analysis is quite large but a null amplitude is always excluded at the 1σ level. No trend is found either with the redshift or dust luminosity. The mean

value $\langle E_b \rangle = 1.26 \pm 0.30$ corresponds to 35% of the amplitude of the bump in the average extinction curve of the MW and to 76% of that in the LMC2 supershell (we are dealing with attenuation curves and not extinction ones). Noll et al. (2009a) measured the amplitude of the UV bump in 68 spectra of galaxies with $1.5 < z < 2.5$ as part of the GMASS survey with a formalism similar to the one used here. They detected robustly a UV bump for 24% of their sample with $E_b = 0.9 \pm 0.1$ and $E_b = 0.5 \pm 0.3$ for the remaining 76% of their sample. Our result is marginally consistent with the mean amplitude they measured for their robust detections of a UV bump.

The *FWHM* of the bump is found to be $356 \pm 20 \text{ \AA}$, midway between the values found in the MW (and the LMC) and in galaxies at $z \sim 2$ (Noll et al. 2009a). The mean slope of the attenuation curve, δ , is found to be -0.13 ± 0.12 and no trend is found for δ as a function of E_b as shown in Fig. 5. Our result is marginally consistent with the Calzetti et al. law that corresponds to $\delta = 0$.

4.2. X-ray emitters

Extinction curves of AGN and quasars are found to not display the 2175 \AA feature, and the wavelength dependence of the extinction in these objects remains controversial between a grey or SMC-like extinction (Li 2007, and references therein). Two of the seven galaxies in our initial sample classified as X-ray emitters by Cardamone et al. (2010), N-17 and N-25, are discarded because of the bad fitting of their SEDs (see discussion in Sect. 3). The SED-fitting process gives amplitudes of the bump for the five remaining sources that are different from 0 but in general lower than for non X-ray galaxies (Fig. 4). We can quantify this difference: for a Gaussian probability distribution of the parameter E_b , $E_b/\text{err}_{E_b} > 2$ corresponds to $E_b > 0$ with a probability of 95% (err_{E_b} is the standard deviation of the distribution).

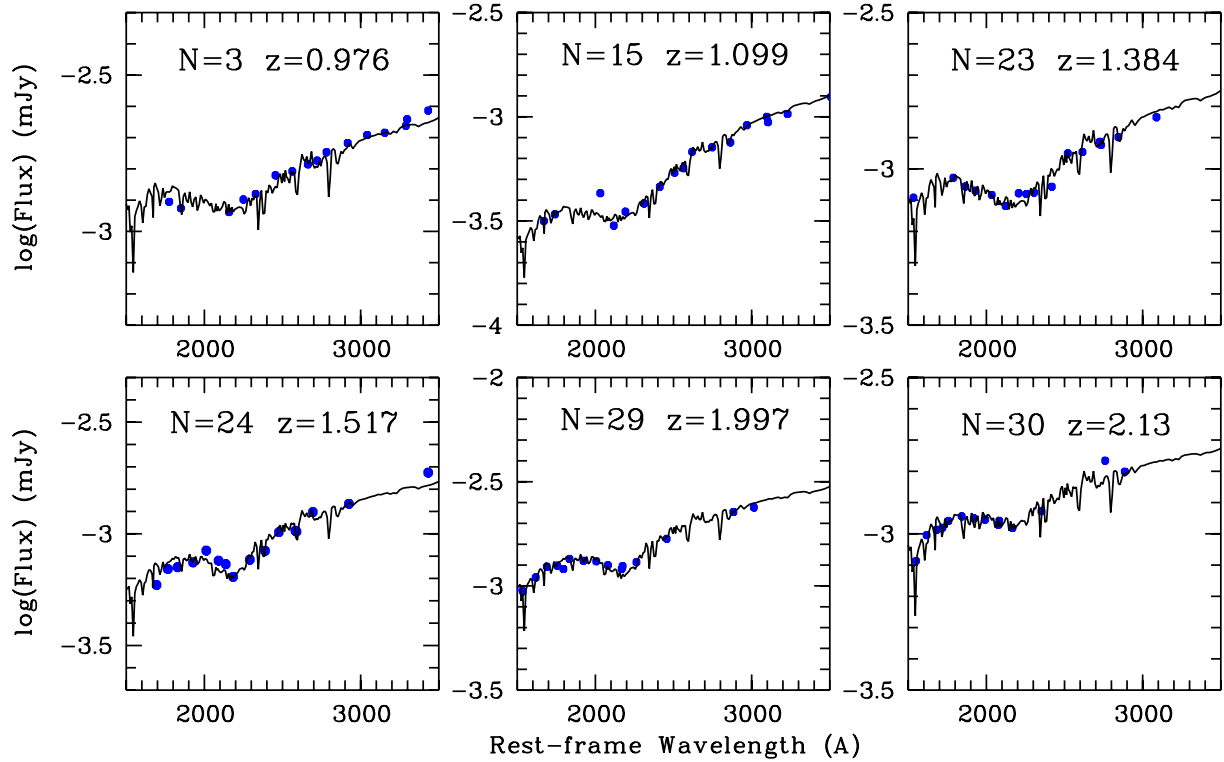


Fig. 3. Spectral energy distributions for $\lambda < 3500 \text{ \AA}$ for the same objects as in Fig. 2. The units, symbols and lines are the same as in Fig. 2 except for the scale of the x-axis, which is now linear.

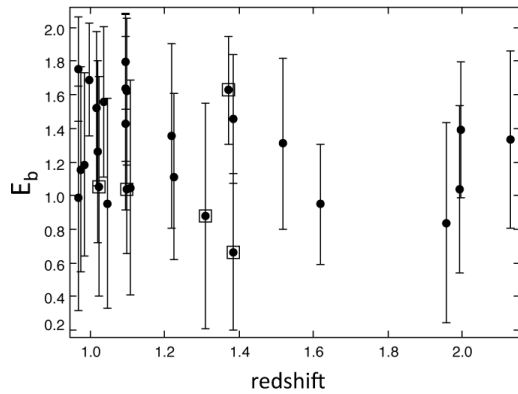


Fig. 4. Amplitude estimated by our Bayesian analysis plotted as a function of the redshift of the sources. Galaxies emitting in X-rays are plotted with empty squares. Standard deviations are reported as error bars.

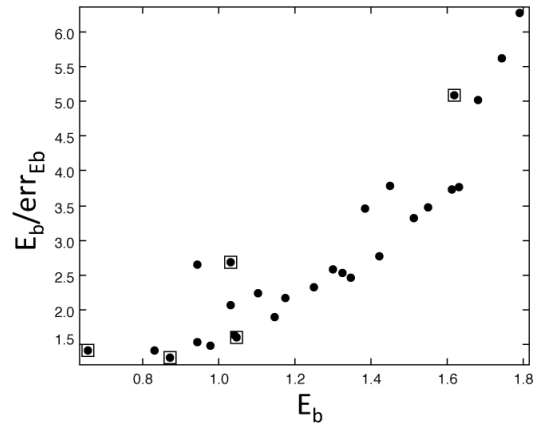


Fig. 6. $\langle E_b \rangle$, the mean value of E_b , divided by its standard deviation err_{E_b} versus $\langle E_b \rangle$. $E_b/err_{E_b} > 2$ corresponds to $E_b > 0$ with a probability of 95%. X-ray galaxies are surrounded with squares.

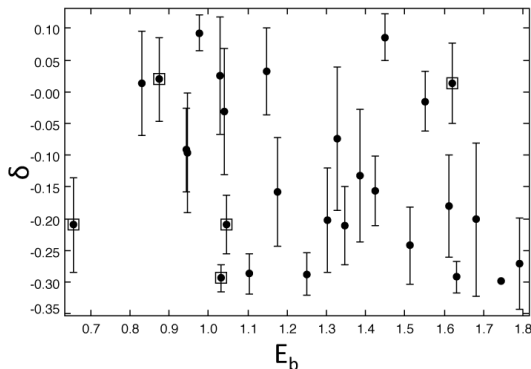


Fig. 5. δ versus the amplitude of the bump E_b . X-ray emitters are surrounded with squares.

Only two out of five X-ray galaxies fulfill this condition compared to 19 of the 23 non X-ray galaxies (Fig. 6). For the first one, N-14 (MUSYCID-30046), $E_b/err_{E_b} = 2.7$. This galaxy has a high X-ray luminosity, $\log(L_X/L_\odot) = 44.1$ with a hardness ratio equal to 0.63 (Cardamone et al. 2008). The fit is of average quality with $\chi^2_{\min} = 4.56$ and the presence of a bump is not obvious from a visual inspection of the SED. It is at least partly because the best-fit model corresponds to a large width of the bump: 500 \AA . The second one is N-21 (MUSYCID-55660). This galaxy (G02:638) is detected in the hard X-rays with an SNR of 2 by Giacconi et al. (2002) when only using SExtractor and not with a method based on wavelet transform. Alexander et al. (2003) did not detect this source, so the X-ray detection may be spurious. Its SED shows a clear absorption feature at 2175 \AA

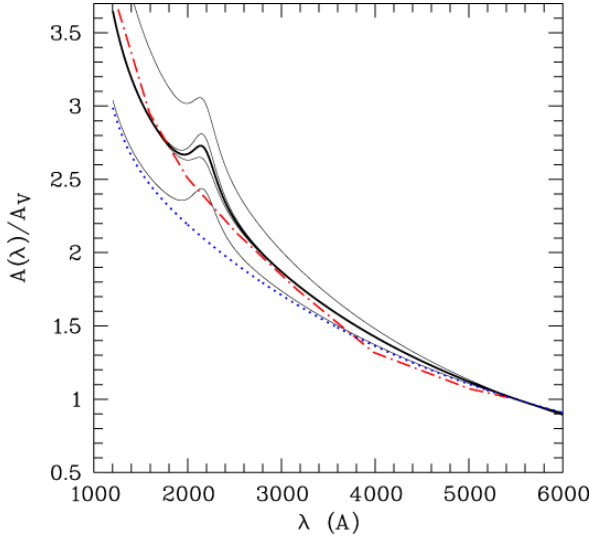


Fig. 7. Average dust attenuation curve. The mean curve found in this work is plotted as a thick line. The thin lines correspond to variations of $\pm 1\sigma$ of the amplitude of the bump, E_b and the slope of the continuum δ ; see text for details. The Calzetti et al. (2000) attenuation curve (dotted blue line) and the effective absorption curve of Charlot & Fall (2000) for a starburst age of 3×10^8 years (dot-dashed red line) are shown in the figure for comparison.

with $E_b/err_{E_b} = 5.1$, and the SED fitting is good ($\chi^2_{\min} = 1.71$). Given the few X-ray sources in our sample, as well as the uncertainties inherent to the two sources for which a bump is measured above 2σ , we cannot draw any firm conclusion about the presence of a UV bump in the attenuation curve of X-ray galaxies.

The slope of the attenuation curve, δ , is found ≈ 0 for two X-ray sources and ≈ -0.2 for the three other ones. Therefore a steep attenuation curve is favoured but is not as steep as the SMC extinction curve and excludes a grey extinction, which corresponds to positive values of δ .

4.3. Average dust attenuation curve

The resulting mean dust attenuation curve obtained for the whole sample is plotted in Fig. 7. All parameters are calculated by a Bayesian analysis. The average dust attenuation curve we obtain can be written as

$$\frac{A(\lambda)}{A_V} = \frac{k'(\lambda) + D_{\lambda_0, \gamma, E_b}(\lambda)}{4.05} \left(\frac{\lambda}{\lambda_V} \right)^{-0.13}, \quad (3)$$

where $\lambda_V = 5500 \text{ \AA}$, $k'(\lambda)$ is given in Calzetti et al. (2000) (Eq. (4)), and

$$D_{\lambda_0, \gamma, E_b}(\lambda) = \frac{1.26 \times 356^2 \lambda^2}{(\lambda^2 - 2175^2)^2 + \lambda^2 \times 356^2}. \quad (4)$$

Strictly speaking, this average attenuation curve only applies to the young stellar component (as explained in Sect. 3), the dust attenuation applied to the old component being reduced by a factor 2. In practice, the SEDs of our galaxies appear to be dominated by the young stellar component (modelled as a constant star formation rate over $\sim 10^8$ years), especially in UV. As a result the global attenuation curve is found to be quite similar to that of the young stellar component alone.

The uncertainty on the average value of δ implies quite a large dispersion of the attenuation curve at $\lambda < 2500 \text{ \AA}$

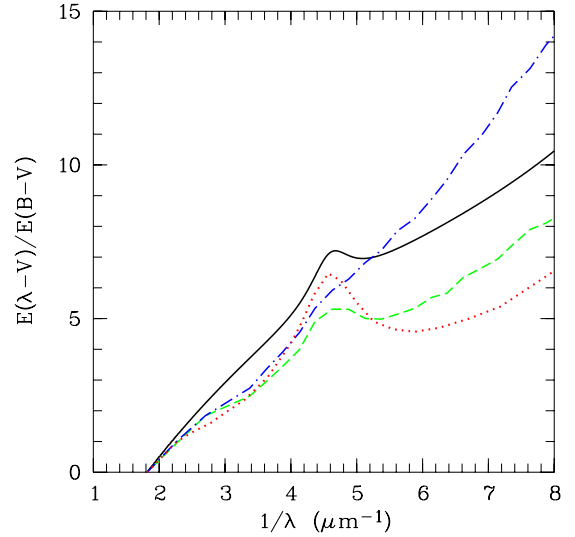


Fig. 8. $E(\lambda - V)/E(B - V)$. The mean curve found in this work is plotted as a thick line, together with the extinction curve of the MW (red dotted line) from Whittet (2003), LMC2 supershell (green short dashed line), and SMC (blue dot-dashed line) from Gordon et al. (2003).

(Fig. 7) and of the determination of dust attenuation at UV wavelengths. For a visual attenuation $A_V = 1 \text{ mag}$, the difference between the dust attenuation at 1500 \AA obtained by using Eq. (3) ($\delta = -0.13$) or a Calzetti et al. law ($\delta = 0$) reaches 0.5 mag . A value of $\delta \neq 0$ also implies a change in the value of the effective total obscuration $R_V = A_V/E_{B-V}$. Calzetti et al. (2000) obtain $R_V = 4.05 \pm 0.80$ by comparing the predicted and observed absorbed emission (i.e. by performing an energetic budget). Adopting a value of $\delta = -0.13$ leads to $R_V = A_V/E_{B-V} = 3.7$, still consistent with the value found by Calzetti et al. (2000). The introduction of a bump of moderate amplitude in the dust attenuation curve (Eq. (3)) leads to an increase of $A(\lambda)/A_V$ at $\approx 2000 \text{ \AA}$ of $\approx 0.35 \text{ mag}$ as compared to the same curve with $D_{\lambda_0, \gamma, E_b}(\lambda) = 0$.

We can compare our average dust attenuation curve to other attenuation curves in the literature. Charlot & Fall (2000) propose a recipe consisting in attenuating the stellar emission by a factor proportional to $\lambda^{-0.7}$, and in reducing the normalization of the attenuation for stars older than 10^7 years. The resulting effective absorption curve they obtain for a constant star formation rate over 3×10^8 years (their Fig. 5) is reported in Fig. 7. A period of 3×10^8 years is close to the mean duration of the burst of star formation we obtain for the young stellar population (10^8 years, cf. Sect. 3). Apart from the presence of the bump, not considered by Charlot & Fall (2000), our mean attenuation curve and that of Charlot & Fall (2000) exhibit similar shapes and steepening for decreasing wavelengths.

Although we are dealing with attenuation and not extinction, we also compare our resulting curve with the extinction curves found in the Milky Way and the Magellanic Clouds. The relative extinctions are compared in Fig. 8. The general shape of the extinction curve of the LMC2 supershell is consistent with our attenuation curve, whereas the MW and SMC extinction curves show flatter and steeper variations, respectively, at short wavelengths.

The exact shape of the extinction curve (slope in the UV range and amplitude of the bump) cannot be constrained with the present data since the attenuation curve we derive strongly

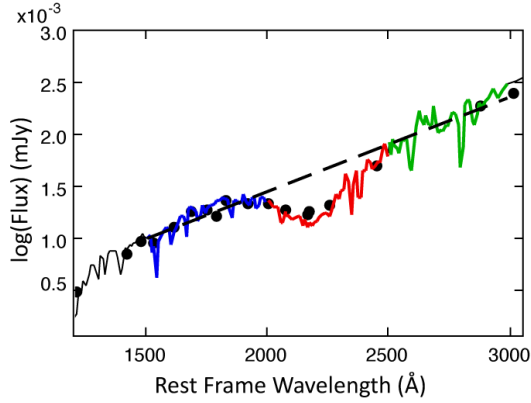


Fig. 9. Definition of 3 bands for ID 2733. The best model found for this galaxy is plotted and the range of wavelengths corresponding to B1, B2, and B3, is in blue, green, and red, respectively. The black dots are the observed fluxes.

depends on the distribution of both stars and dust. Witt & Gordon (2000) show that the shape of the attenuation function also depends on the total amount of dust attenuation. We do not observe any variation in E_b and δ with A_{UV} and it can be explained by the homogeneity of our sample in terms of dust attenuation associated to the large uncertainties on the determination of these parameters. Radiative transfer models in opaque disks with various configurations of stars and dust (especially in a clumpy medium) are able to reduce the amplitude of the UV bump in the effective attenuation with a dust composition similar to that of the MW or the average LMC, the attenuation curve becoming greyer when the opacity increases (e.g. Witt & Gordon 2000; Pierini et al. 2004; Inoue et al. 2006; Panuzzo et al. 2007). These models also predict a flattening of the attenuation curve in UV (as an effect of the grey attenuation) as compared to the original extinction curve. The average attenuation curve we deduce increases steeply at short wavelengths. It seems to favour the scenario of a deficiency of bump carriers with respect to the case of MW or average LMC. We see in Sect. 5.2 that our sources roughly follow the A_{UV} - β relation found by Meurer et al. (1999) for local starbursts that is explained well by a clumpy shell geometry (Witt & Gordon 2000; Calzetti 2001). Such a dust/star configuration favours the interpretation of a moderate UV bump in the extinction curve itself, in agreement with our conclusion (e.g. Witt & Gordon 2000; Noll et al. 2009a).

5. Slope of the UV continuum from broad band photometry and dust attenuation

5.1. Determination of the UV slope

With the imprint of the UV bump clearly visible in our sample, the assumption of a simple power law for the entire UV continuum is no longer valid, and its influence on the measured slopes can be quantified.

5.1.1. Influence of the bump

A single power law to model the UV continuum might be valid if we exclude the spectral region of the bump (Fig. 3). Since our fluxes are defined in Jansky we define α as $f_\nu \propto \lambda^\alpha$ with $\alpha = \beta + 2$ where β corresponds to the original definition $f_\lambda(\text{erg cm}^{-2} \text{s}^{-1} \text{Å}^{-1}) \propto \lambda^\beta$. From Fig. 3 it is clear that we can extend the model of a power law up to 3000 Å. Therefore we

calculate the slope of the UV continuum in several ways. First we use all the data between 1200 and 3000 Å, avoiding the bump range (1975–2375 Å) and perform a linear regression. The resulting value of α will be taken as our reference α_{ref} . Then we define three wavelength ranges 1500–2000 Å (B1), 1500–2500 Å (B2) and 2500–3000 Å (B3) that mimic broad band filters and combine two of these bands to estimate α . The definition of these three bands is illustrated in Fig. 9 for a galaxy exhibiting a strong bump. B2 overlaps the bump, therefore we expect some effects when the slope is calculated by considering it. The slopes of the UV continuum are calculated following the prescription of Kong et al. (2004) adapted to our notation:

$$\alpha = \frac{\log(f_{\nu_i}/f_{\nu_j})}{\log(\lambda_i/\lambda_j)} \quad (5)$$

where f_{ν_i} and f_{ν_j} are the mean flux densities per unit frequency through the filters i and j whose effective wavelengths are λ_i and λ_j . In Fig. 10 the α values obtained by combining B1 and B2 (α_{12}), B2 and B3 (α_{23}) and B1 and B3 (α_{13}) are compared to α_{ref} measured on the entire UV SED. As expected α_{13} which are calculated by avoiding the bump, is found to correlate very well with α_{ref} (Fig. 10 top panel, $R = 0.92$). The combination of B1-B2 leads to bluer slopes, whereas the slopes calculated with B2 and B3 are redder than α_{ref} . These effects are expected since the presence of the bump increases the dust attenuation in the B2 band. The amplitude of the shifts are $\langle \alpha_{12} - \alpha_{\text{ref}} \rangle = -0.46 \pm 0.26$ and $\langle \alpha_{23} - \alpha_{\text{ref}} \rangle = 0.28 \pm 0.40$, whereas $\langle \alpha_{13} - \alpha_{\text{ref}} \rangle = -0.09 \pm 0.25$.

5.1.2. GALEX-like UV slope

The FUV and NUV bands of GALEX are commonly used to measure the slope of the UV continuum in the nearby universe (e.g. Seibert et al. 2005). Since the NUV band (1771–2831 Å) (Morrissey et al. 2005) overlaps the UV bump we might expect some underestimation of the slopes. The quantity α_{GALEX} is an output of CIGALE: the SED of each model generated by the code is integrated in the FUV and NUV (rest frame) filter bands and α_{GALEX} calculated with the above formula. Then the expected value of α_{GALEX} for each galaxy of our sample is estimated through a Bayesian calculation (Giovannoli et al. 2011). The correlation between α_{GALEX} and α_{ref} is very good ($R = 0.91$). As expected, α_{GALEX} is typically lower (bluer) than α_{ref} but the systematic difference remains small with $\langle \alpha_{\text{GALEX}} - \alpha_{\text{ref}} \rangle = -0.19 \pm 0.24$. This moderate shift, which is less than the one found considering α_{12} , is probably due to the wide large bandpass of the NUV filter (1060 Å, Morrissey et al. 2005), much wider than the bump itself. Therefore, as long as galaxies exhibit a bump in their attenuation curve similar to that found in this study (1/3 that of the Milky Way), the slopes measured with the GALEX data are found to be reliable. Burgarella et al. (2005) show that Milky Way-like bumps have a strong influence on the determination of the UV slope with GALEX filters.

5.1.3. Impact of photometric errors

It is worth noting that the determination of the UV slope through two broad band filters is very sensitive to photometric errors, as well as to the interval between the effective wavelengths of both filters i.e. the factor $\log(\lambda_i/\lambda_j)$ in Eq. (3). We can rewrite Eq. (3) in terms of magnitudes instead of fluxes:

$$\alpha = \beta + 2 = -0.4 \frac{(m_i - m_j)}{\log(\lambda_i/\lambda_j)} \quad (6)$$

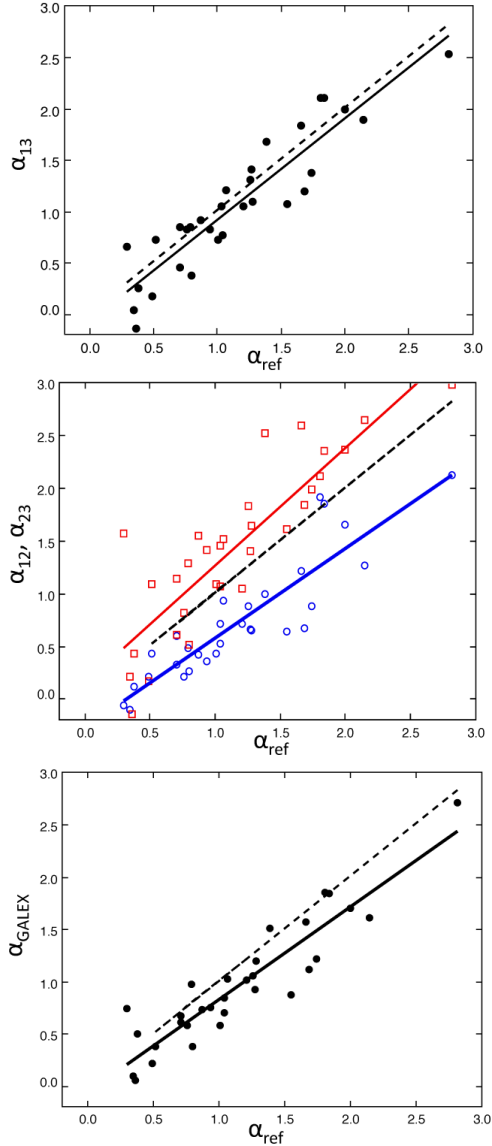


Fig. 10. Various estimates of α compared to the reference value α_{ref} measured on the full SED, *top*: α_{13} versus α_{ref} ; *middle*: α_{12} (blue empty circles) and α_{23} (red empty squares) versus α_{ref} ; *bottom*: α_{GALEX} calculated with the rest frame FUV and NUV fluxes versus α_{ref} . In each figure, the dashed lines represent the 1:1 line, the solid lines are the results of linear regressions.

Using the FUV and NUV filters of GALEX, the relation becomes $\alpha = -2.22(m_i - m_j)$, and a typical error of 0.1 mag in FUV and NUV translates to an error of 0.3 on α . It is obvious from Eq. (6) that increasing the wavelength difference between the two filters reduces the uncertainty on the determination of α and β . For the domain of validity of the power law adopted in this work ($\lambda < 3000 \text{ \AA}$, cf. Sect. 5.1.1), using filters with the largest possible interval between rest frame wavelength, i.e. 1300 \AA (to avoid the flattening of the attenuation curve for $\lambda \leq 1200 \text{ \AA}$; Leitherer et al. 2002; Buat et al. 2002), and 3000 \AA reduces the error by a factor ~ 2 (this time $\alpha = -1.11(m_i - m_j)$) as compared to the use of GALEX filters.

To summarize, given the uncertainty on the presence and strength of a UV bump in a galaxy, one must avoid the region affected by the bump as much as possible when measuring the UV slope using broad band filters and use filters with effective

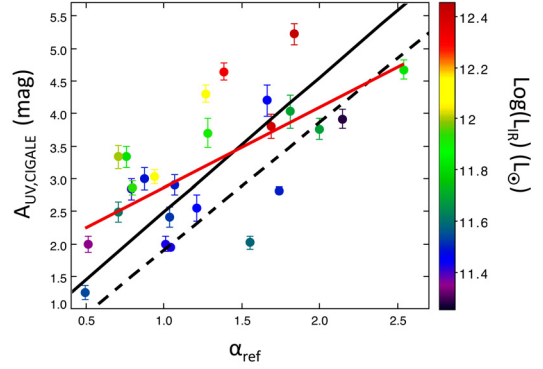


Fig. 11. UV dust attenuations from CIGALE plotted against the slope of the UV continuum calculated with the full SED. The total IR luminosity is colour-coded. The solid and dashed lines correspond to the inner and total relations of Overzier et al. (2011) respectively. The error bars come from CIGALE (Bayesian estimates of the parameters and their associated errors). The red line is the result of the linear regression.

wavelengths that are as widely separated as possible from each other. If the region of the bump cannot be avoided, the attenuation curve presented in Eq. (3) might be used to interpret the data.

5.2. Dust attenuation corrections

Meurer et al. (1999) first deduced a relation between A_{UV} and β for local starbursts, avoiding the bump area on the spectra obtained with IUE. Several calibrations have been proposed since this pioneering work (Calzetti et al. 2000; Seibert et al. 2005; Overzier et al. 2011). One issue of the preliminary analyses was that the UV data came from IUE, whose aperture sampled only the inner part of the galaxies. Overzier et al. (2011) re-investigate the topic by using GALEX images defining an ‘inner and total’ relation, the first one based on UV fluxes measured into an IUE-like aperture, the second one corresponding to the total UV fluxes. These relations are

$$A_{\text{UV}} = 4.54 + 2.07\beta = 4.54 + 2.07(\alpha - 2)$$

for the inner relation and

$$A_{\text{UV}} = 3.85 + 1.96\beta = 3.85 + 1.96(\alpha - 2)$$

for the total relation. In Fig. 11 these relations are compared to the values of α_{ref} and $A_{\text{UV,CIGALE}}$ (the dust attenuation obtained from the SED fitting process and a Bayesian calculation). Whereas LIRGs seem to follow more or less the local starburst relations, the ULIRGs are found above the local relations, which agrees with previous studies at low and high redshifts (Takeuchi et al. 2010; Howell et al. 2010; Burgarella et al. 2007; Reddy et al. 2008). Buat et al. (2010) performed a selection at $250 \mu\text{m}$ at $z < 0.3$ and found that their sample (including LIRGs) lie below the local starburst relation. This different behaviour is likely to be a selection effect biased towards more quiescent galaxies when selected at $250 \mu\text{m}$ than in the mid-IR or around $60 \mu\text{m}$ and to the use of the GALEX colour to measure the UV slope at $z > 0$.

A linear regression on the whole sample gives

$$A_{\text{UV,CIGALE}} = 1.46 (\pm 0.21) \alpha_{\text{ref}} + 1.50 (\pm 0.29) \quad (7)$$

with a correlation coefficient $R = 0.79$. The correlation is rather weak, resulting in a large dispersion with an rms scatter of

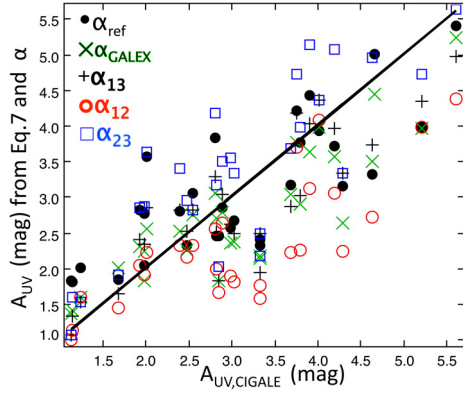


Fig. 12. Comparison of UV dust attenuations: the values of A_{UV} directly obtained from the SED fitting with CIGALE are plotted on the x -axis and the estimates of A_{UV} from different UV slopes and Eq. (7) on the y -axis.

0.73 mag. This error directly affects any estimate of L_{IR} based on relations between L_{IR}/L_{UV} , which is a quantity tightly related to A_{UV} (Buat et al. 2011, and references therein), and the slope of the UV continuum.

We can also compare dust attenuation corrections obtained by applying Eq. (7) to the various estimates of α defined in Sects. 5.1.1 and 5.1.2. The results are reported in Fig. 12 and compared to the dust attenuation given by CIGALE: $A_{UV,CIGALE}$. A large dispersion is found as a consequence of the loose relation found initially between A_{UV} and α_{ref} (Fig. 11): $\langle A_{UV,\alpha_{ref}} - A_{UV,CIGALE} \rangle = -0.005 \pm 0.707$ mag. When using α_{13} the systematic shift remains moderate $\langle A_{UV,\alpha_{13}} - A_{UV,CIGALE} \rangle = -0.18 \pm 0.58$ mag. The quantities α_{GALEX} , α_{12} , and α_{23} give worse estimates with substantial shifts and large dispersions: $\langle A_{UV,\alpha_{GALEX}} - A_{UV,CIGALE} \rangle = -0.32 \pm 0.58$ mag, $\langle A_{UV,\alpha_{12}} - A_{UV,CIGALE} \rangle = -0.73 \pm 0.70$ mag, and $\langle A_{UV,\alpha_{23}} - A_{UV,CIGALE} \rangle = 0.37 \pm 0.71$ mag.

Therefore, using UV slopes derived from broad band colours leads to large uncertainties in the derivation of dust attenuation (~ 1 mag) even if the bump area is avoided and good photometry is available. This is due to the intrinsic dispersion found between the slope of the UV continuum and the amount of dust attenuation. The presence of a bump in one of the filters may add a systematic shift that can reach 0.7 mag for the galaxies of our sample, which is likely to be representative of star-forming galaxies at redshifts between 1 and 2. These results hold for galaxies with a moderate bump in their dust attenuation curve (35% of the mean amplitude found in the MW), and we expect larger effects for larger bumps.

6. Conclusions

We have identified a UV bump in a sample of galaxies of the CDFS at redshifts between $0.9 < z < 2.2$, selected to be observed in intermediate and broad band optical filters, as well as at mid- and far-IR wavelengths by *Spitzer* and *Herschel*. This study demonstrates the capabilities of intermediate-band photometry to give details on the SED of galaxies and to derive physical properties.

The average dust attenuation curve we deduce is described well by a modified Calzetti et al. law slightly steeper than the original one and with a UV bump at 2175 \AA whose amplitude is $\sim 35\%$ of the MW one. We propose an analytical expression of the average attenuation curve, which can be used to correct the

SEDs of galaxies for dust attenuation. The moderate amplitude of the bump, together with the substantial slope of our average attenuation curve in the UV, argues for a deficit of UV bump carriers in our sample galaxies as compared to the MW.

Our sample contains seven X-ray galaxies. Five of them are reasonably fitted: a steep attenuation curve is favoured as excluding a grey extinction. The sample is too small to draw any firm conclusion about the presence of a UV bump. In all cases the amplitude of the bump, if any, is smaller than found for non X-ray galaxies.

The presence of a bump in the mean dust attenuation curve has implications for deriving the slope of the UV (rest frame) continuum of galaxies from broad band data alone. The power law modelling of the UV spectral distribution of our galaxies can be extended up to 3000 \AA , but the bump area must be avoided. When a broad band filter overlaps the bump, despite its moderate amplitude, the error on the determination of the slope may reach ~ 0.5 . The use of GALEX filters leads to an underestimation of the slope by only 0.2, even if the NUV filter overlaps the bump. This is likely because of the very large bandpass of this filter. However, the proximity of the two central wavelengths of the GALEX filters implies a large uncertainty in determining the slope. We stressed that a larger wavelength baseline would give a better measure.

Dust attenuation estimated with UV slopes, even reliable ones, remains uncertain, with an RMS error of 0.7 mag.

Acknowledgements. This work is partially supported by the French National Agency for research (ANR-09-BLAN-0224). PACS has been developed by a consortium of institutes led by MPE (Germany) and including UVIE (Austria); KU Leuven, CSL, IMEC (Belgium); CEA, LAM (France); MPIA (Germany); INAF/IS/OAA/OAP/OAT, LENS, SISSA (Italy); IAC (Spain). This development has been supported by the funding agencies BMVIT (Austria), ESA-PRODEX (Belgium), CEA/CNES (France), DLR (Germany), ASI/INAF (Italy), and CICYT/MCYT (Spain).

References

- Alexander, D. M., Bauer, F. E., Brandt, W. N., et al. 2003, *AJ*, 126, 539
 Buat, V., Burgarella, D., Deharveng, J. M., & Kunth, D. 2002, *A&A*, 393, 33
 Buat, V., Giovannoli, E., Burgarella, D., et al. 2010, *MNRAS*, 409, L1
 Buat, V., Giovannoli, E., Takeuchi, T. T., et al. 2011, *A&A*, 529, 22
 Burgarella, D., Buat, V., & Iglesias-Páramo, J. 2005, *MNRAS*, 360, 1413
 Burgarella, D., Le Floch, E., Takeuchi, T. T., et al. 2007, *MNRAS*, 380, 986
 Calzetti, D. 2001, *PASP*, 113, 1449
 Calzetti, D., Kinney, A. L., & Storchi-Bergmann, T. 1994, *ApJ*, 429, 582
 Calzetti, D., Armus, L., Bohlin, R. C., et al. 2000, *ApJ*, 533, 682
 Charlot, S., & Fall, S. M. 2000, *ApJ*, 539, 718
 Cardamone, C. N., Urry, P. G., Damen, M., et al. 2008, *ApJ*, 680, 130
 Cardamone, C. N., van Dokkum, P. G., Urry, C. M., et al. 2010, *ApJS*, 189, 270
 Cartledge, S. I. B., Clayton, G. C., Gordon, K. D., et al. 2005, *ApJ*, 630, 355
 Conroy, C. 2010, *MNRAS*, 404, 247
 Conroy, C., Schiminovich, D., & Blanton, M. R. 2010, *ApJ*, 718, 184
 Dale, D. A., & Helou, G. 2002, *ApJ*, 576, 159
 Daddi, E., Alexander, D. L., Dickinson, M., et al. 2007, *ApJ*, 670, 156
 Dickinson, M., Giavalisco, M., the GOODS team 2003, in *The Mass of Galaxies at Low and High Redshift*, ed. R. Bender, & Alvio Renzini (Springer), 324
 Draine, B. T. 1989, in *Interstellar Dust*, ed. L. J. Allamandola, & G. G. M. Tielens, *Proc. IAU Symp.*, 135, 313
 Elbaz, D., Daddi, E., Le Borgne, D., et al. 2007, *A&A*, 468, 33
 Elbaz, D., Hwang, H. S., Magnelli, B., et al. 2010, *A&A*, 518, L29
 Elbaz, D., Dickinson, M., Hwang, H. S., et al. 2011, *A&A*, in press
[\[arXiv:1105.2537\]](https://arxiv.org/abs/1105.2537)
 Fitzpatrick, E. L., & Massa, D. 1990, *ApJS*, 72, 163
 Fitzpatrick, E. L., & Massa, D. 2007, *ApJ*, 663, 320
 Fritz, J., Franceschini, A., & Hatziminaoglou, E. 2006, *MNRAS*, 366, 767
 Giacconi, R., Zirm, A., Wang, J., et al. 2002, *ApJS*, 139, 369
 Giovannoli, E., Buat, V., Noll, S., Burgarella, D., & Magnelli, B. 2011, *A&A*, 525, 150
 Gordon, K. D., Clayton, G. C., Misselt, K. A., Landolt, A. U., & Wolff, M. J. 2003, *ApJ*, 594, 279

- Howell, J. H., Armus, L., & Mazzarella, J. M., et al. 2010, *ApJ*, 715, 572
- Inoue, A., Buat, V., Burgarella, D., et al. 2006, *MNRAS*, 370, 380
- Ibert, O., Capak, P., Salvato, M., et al. 2009, *ApJ*, 690, 1236
- Johnson, B. D., Schiminovich, D., Seibert, M., et al. 2007a, *ApJ*, 173, 377
- Johnson, B. D., Schiminovich, D., Seibert, M., et al. 2007b, *ApJ*, 173, 392
- Kong, X., Charlot, S., Brinchmann, J., & Fall, S. M. 2004, *MNRAS*, 349, 769
- Kriek, M., van Dokkum, P. G., Whitaker, K., et al. 2011, *ApJ*, submitted
[arXiv:1103.0279]
- Leitherer, C., Li, I. H., Calzetti, D., & Heckman, T. M. 2002, *ApJS*, 140, 303
- Liang, S. L., & Li, A. 2009, *ApJ*, 690, L56
- Liang, S. L., & Li, A. 2010, *ApJ*, 710, 648
- Li, A. 2007, in *The Central Engine of Active Galactic Nuclei*, ed. L. C. Ho, & J.-M. Wang, ASP Conf. Ser., 373, 561
- Li, A., & Draine, B. T. 2002, *ApJ*, 576, 762
- Meurer, G. R., Heckman, T. M., & Calzetti, D. 1999, *ApJ*, 521, 64
- Melbourne, J., Koo, D., & Le Floch, E. 2005, *ApJ*, 625, L65
- Morrissey, P., Schiminovich, D., Barlow, T. A., et al. 2005, *ApJ*, 619, L7
- Mullaney, J. R., Alexander, D. M., Goulding, A. D., & Hickox, R. C. 2011, *MNRAS*, 414, 1082
- Noll, S., & Pierini, D. 2005, *A&A*, 137, 155
- Noll, S., Pierini, D., Pannella, M., & Savaglio, S. 2007, *A&A*, 472, 455
- Noll, S., Pierini, D., Cimatti, A., et al. 2009a, *A&A*, 499, 69
- Noll, S., Burgarella, D., Giovannoli, E., et al. 2009b, *A&A*, 507, 1793
- Overzier, R., Heckman, T. M., Wang, J., et al. 2011, *ApJ*, 726, L7
- Panuzzo, P., Granato, G. L., & Buat, V. 2007, *MNRAS*, 375, 640
- Pierini, D., Gordon, K. D., Witt, A. N., & Madsen, G. J. 2004, *ApJ*, 617, 1022
- Pilbratt, G., Riedinger, J. R., Passvogel, T., et al. 2010, *A&A*, 518, L1
- Poglitsch, A., Waelkens, C., Geis, N., et al. 2010, *A&A*, 518, L2
- Reddy, N. A., Steidel, C. C., Pettini, M., et al. 2008, *ApJ*, 692, 778
- Seibert, M., Martin, D. C., Heckman, T. M., et al. 2005, *ApJ*, 619, L55
- Siebenmorgen, R., Freudling, W., Krügel, E., & Haas, M. 2004, *A&A*, 421, 129
- Takeuchi, T. T., Buat, V., Heinis, S., et al. 2010, *A&A*, 514, A4
- Vijh, U., Witt, A. N., & Gordon, K. D. 2003, *ApJ*, 587, 533
- Wijesinghe, D. B., Hopkins, A. M., & Sharp, R., et al. 2011, *MNRAS*, 410, 2291
- Whittet, D. C. B. 2003, *Dust in the Galactic environment*, series in Astronomy and Astrophysics (Institute of Physics Publishing)
- Witt, A. N., & Gordon, K. D. 2000, *ApJ*, 528, 799
- Xiang, F. Y., Li, A., & Zhng, J. X. 2011, *ApJ*, 733, 91
- Zafar, T., Watson, D., Fynbo, J. P. U., et al. 2011, *A&A*, 521, A143

Appendix A:

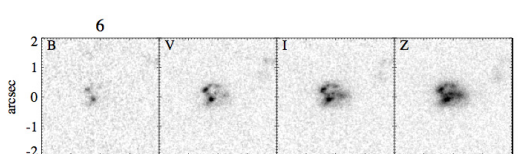
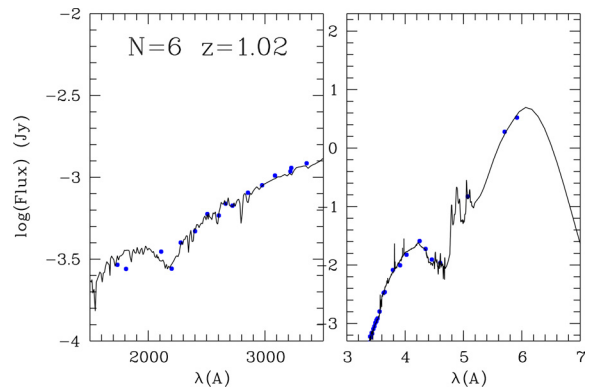
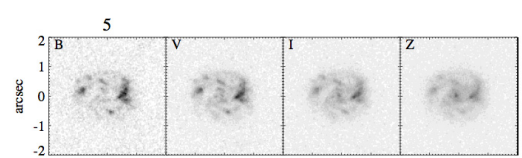
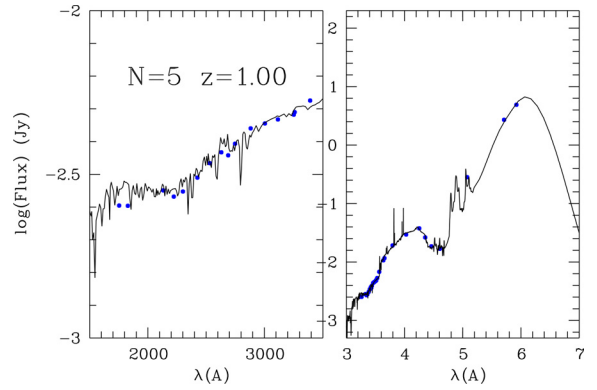
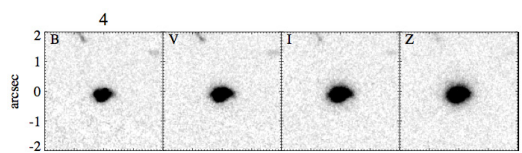
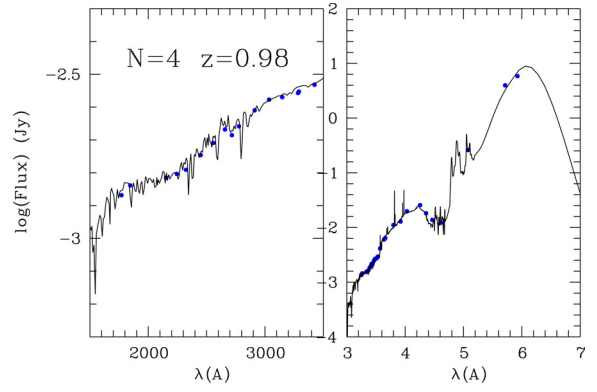
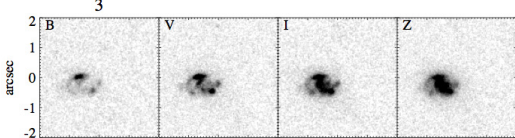
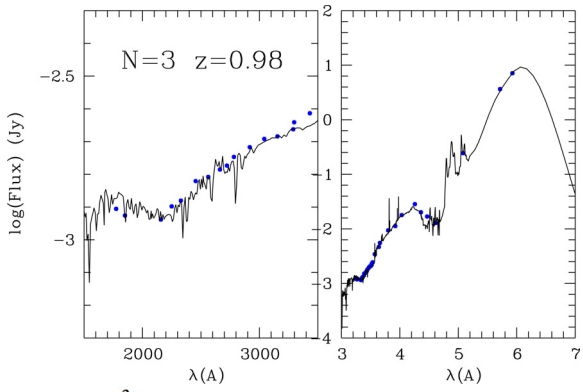
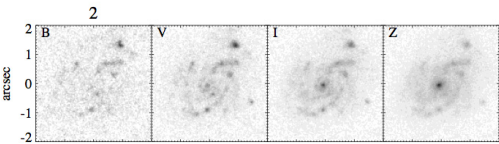
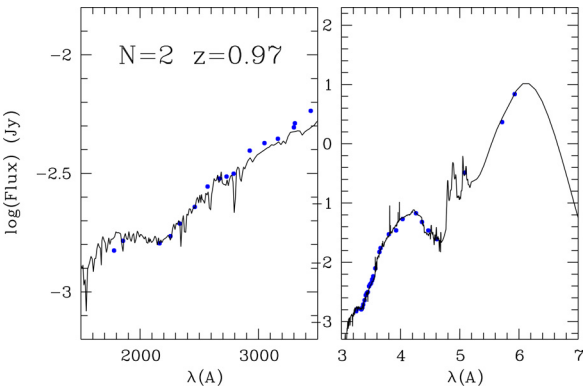
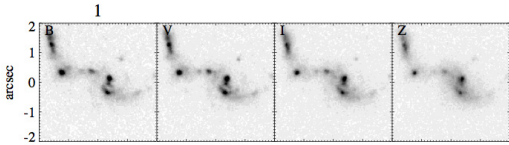
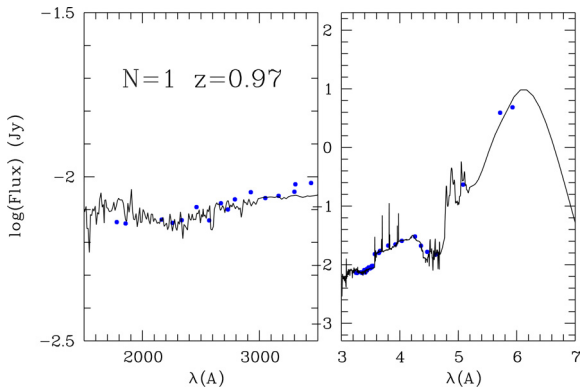


Fig. A.1. Spectral energy distributions for the full sample and HST images obtained from the GOODS cutout service V0.2. The best fit is represented with a solid line. The rest frame wavelength is plotted on the x-axis and the fluxes in Jy on the y-axis.

Fig. A.1. continued.

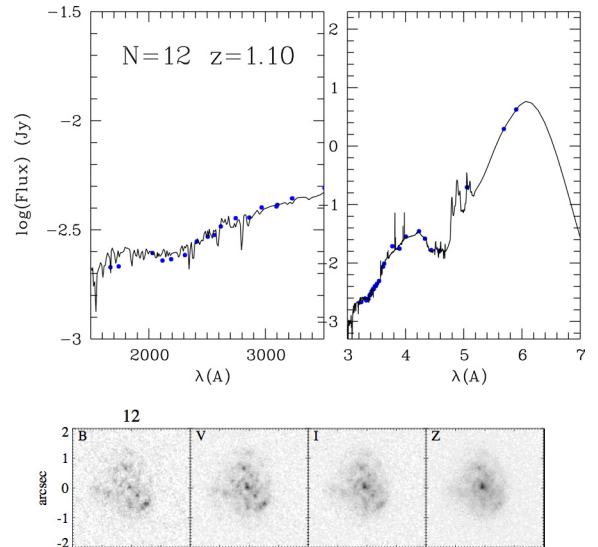
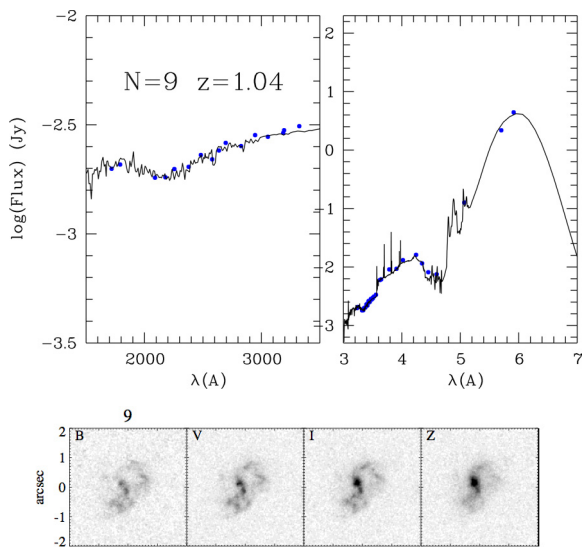
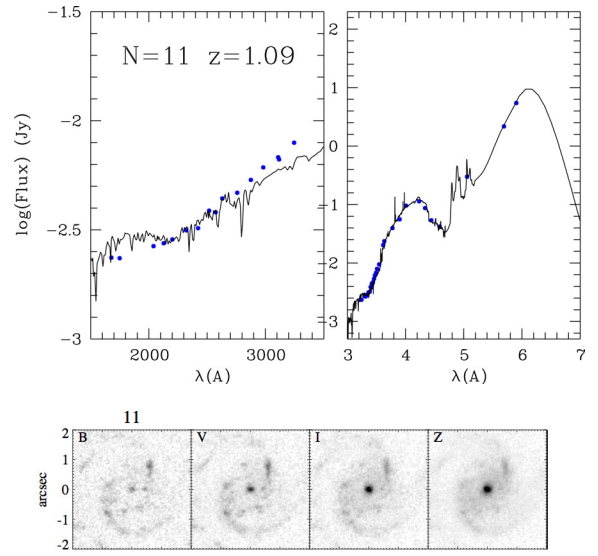
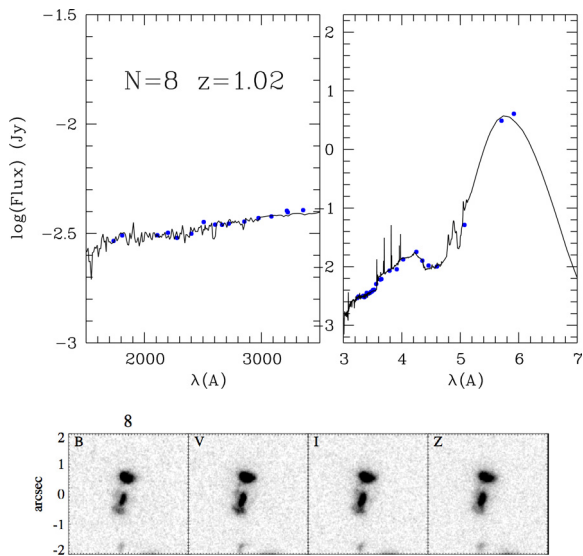
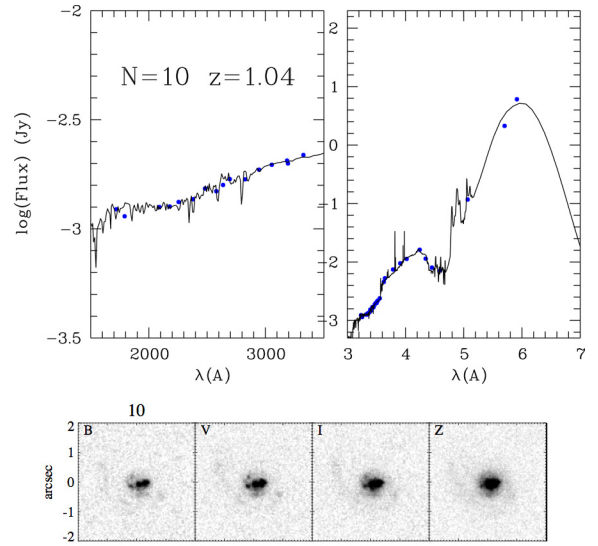
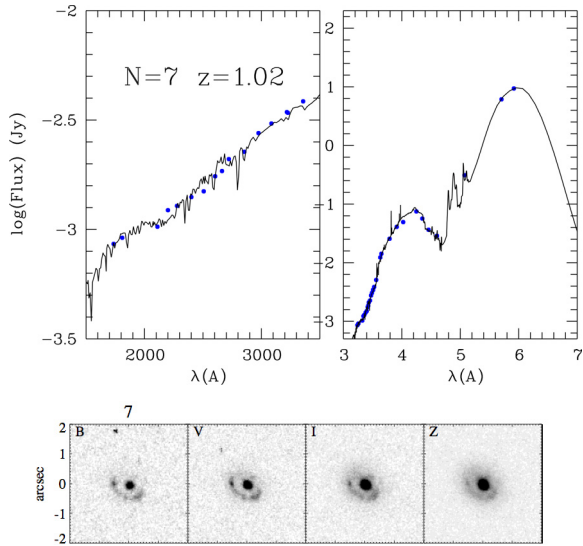


Fig. A.1. continued.

Fig. A.1. continued.

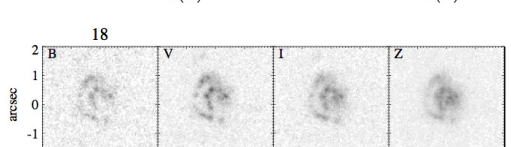
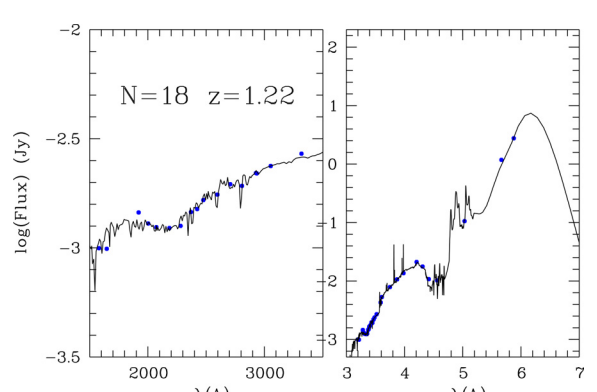
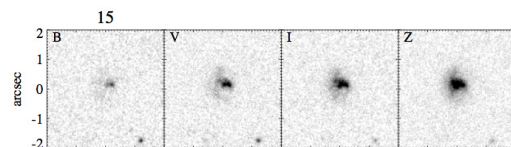
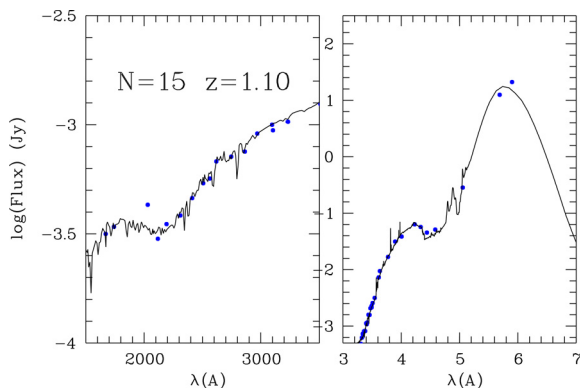
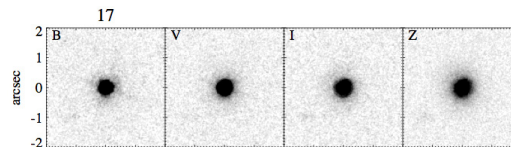
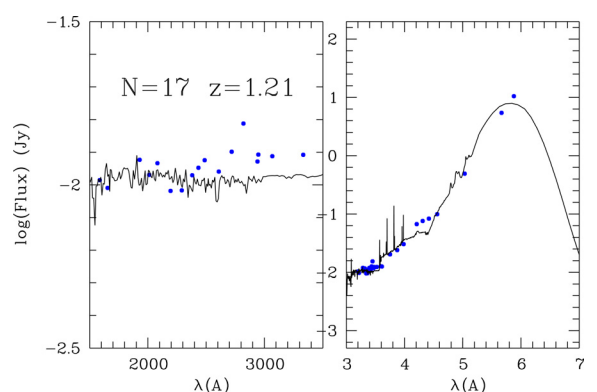
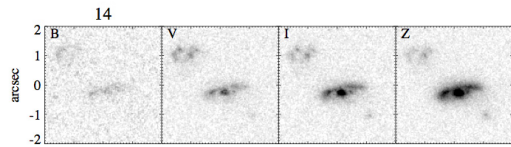
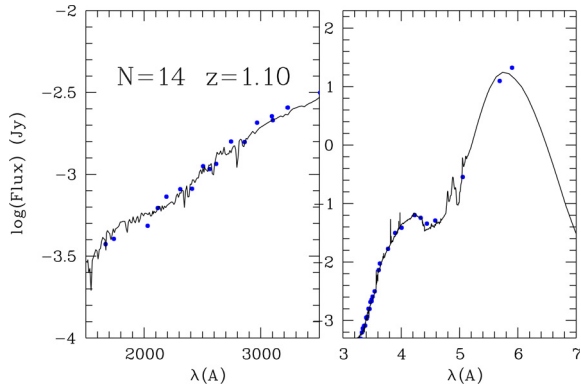
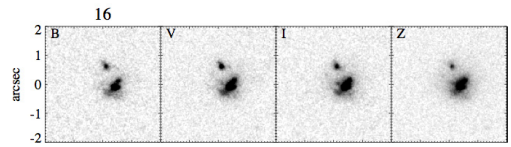
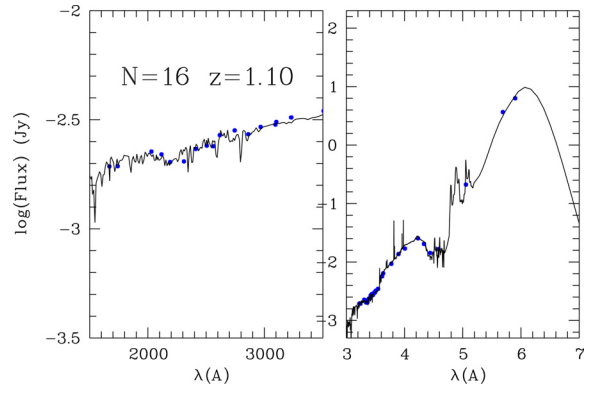
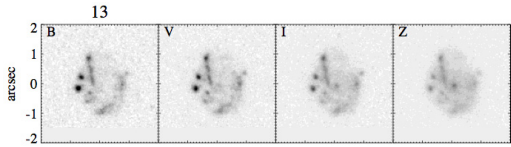
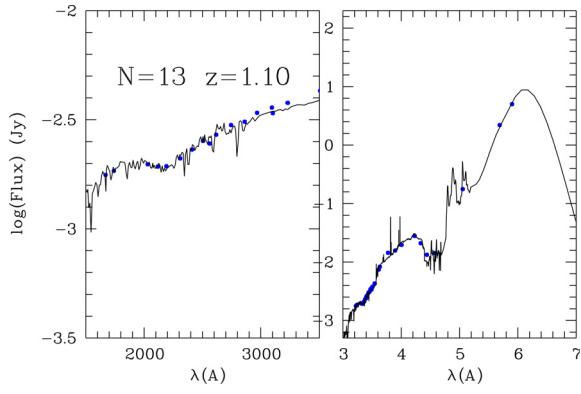


Fig. A.1. continued.

Fig. A.1. continued.

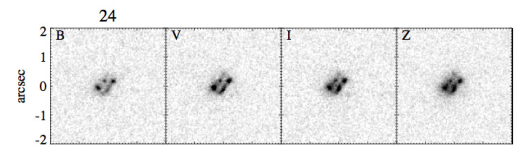
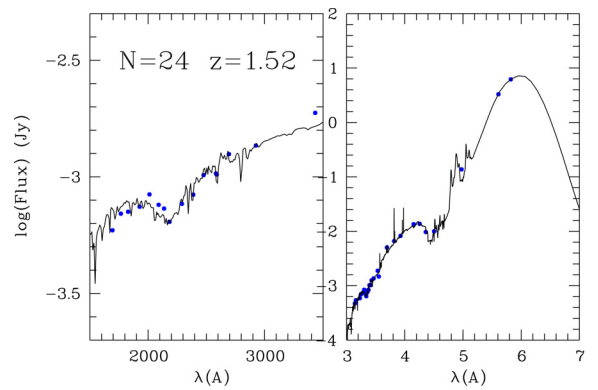
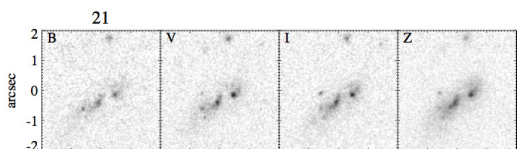
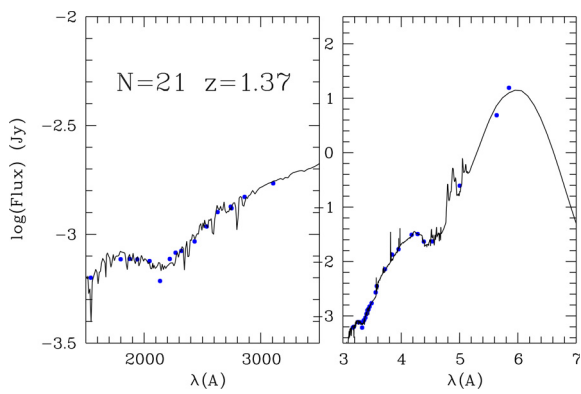
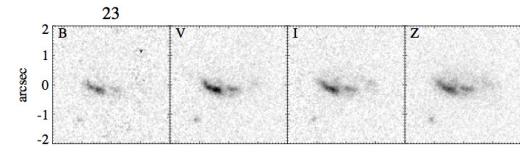
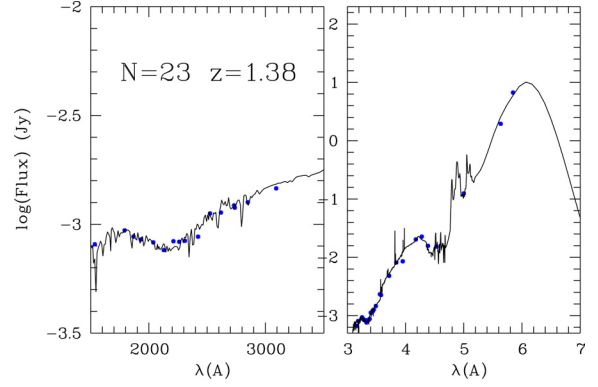
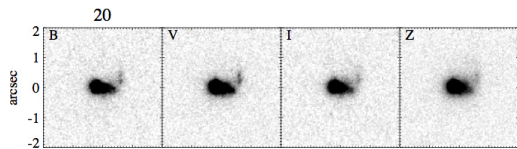
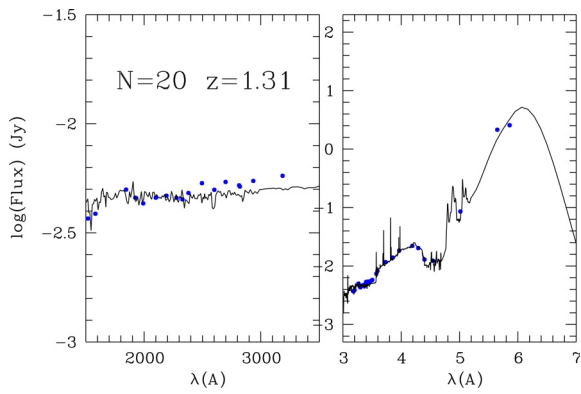
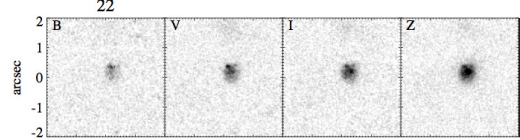
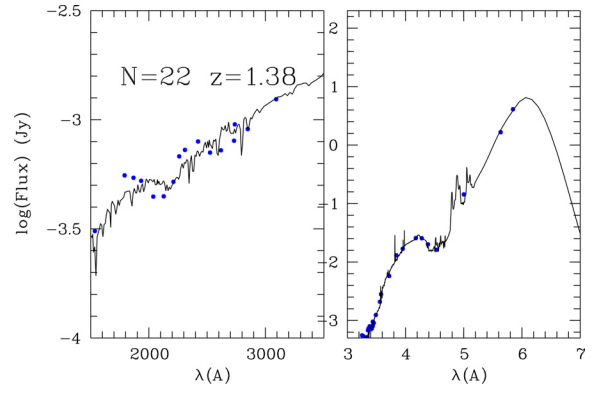
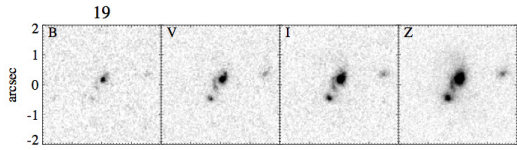
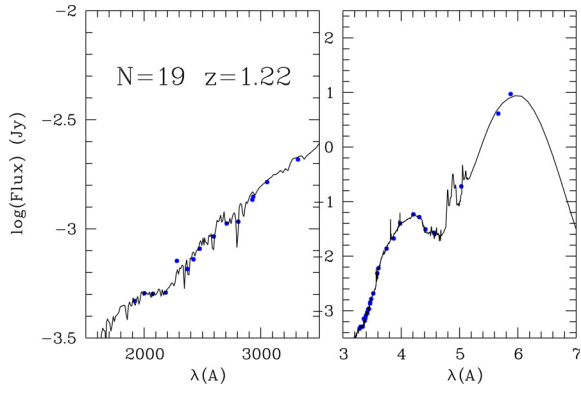


Fig. A.1. continued.

Fig. A.1. continued.

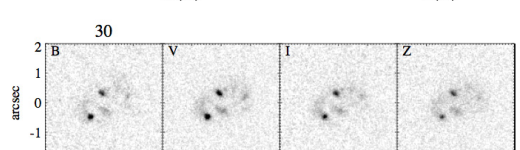
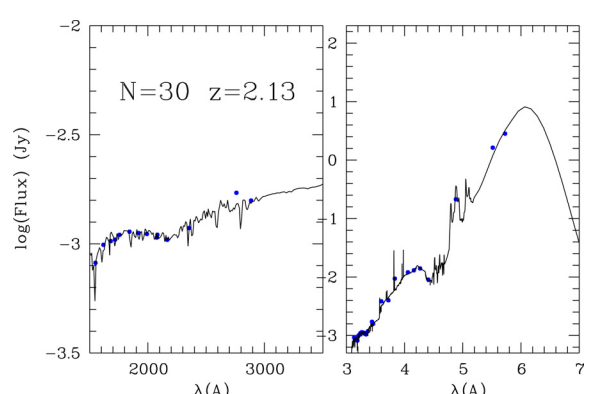
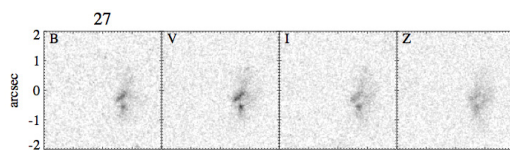
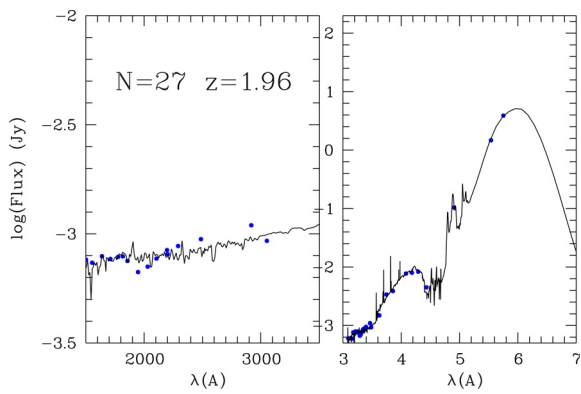
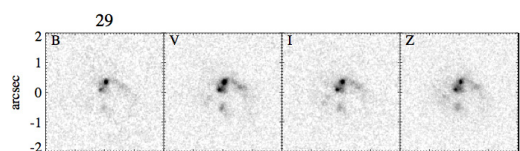
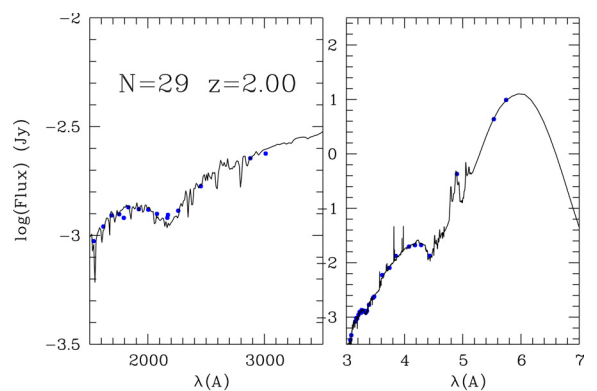
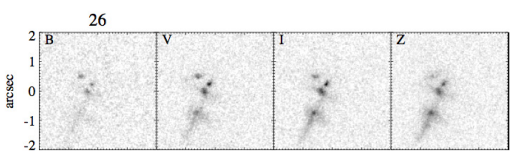
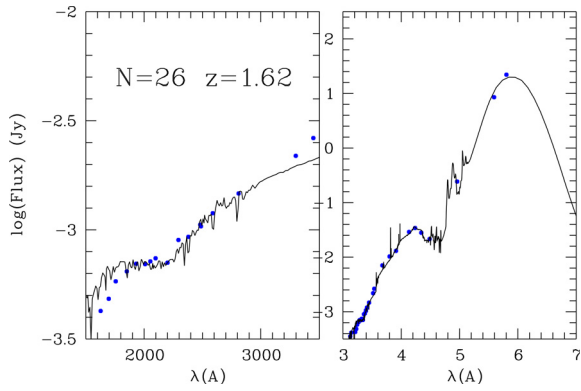
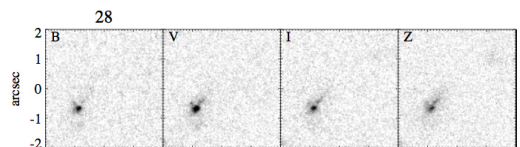
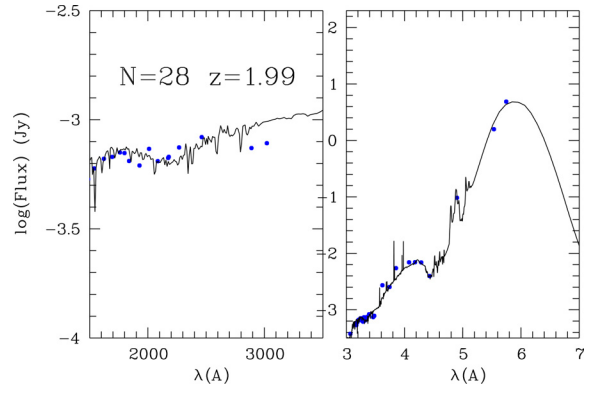
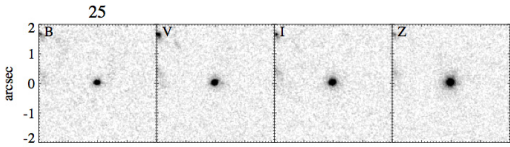
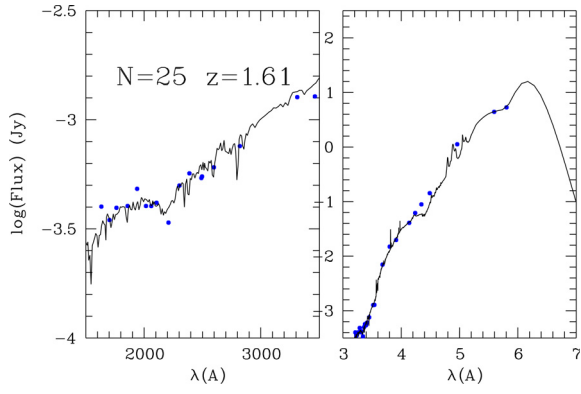


Fig. A.1. continued.

Fig. A.1. continued.